

# **Advection errors and grid dependency in numerical river modelling**

**Comparing codes Telemac, D-Flow FM, UnTRIM and  
Delft3D**

**Project report**

Frank Platzek

Version: 1.0

September 19, 2019

## **Advection errors and grid dependency in numerical river modelling, Project report**

### **Published and printed by:**

Deltares  
Boussinesqweg 1  
2629 HV Delft  
P.O. 177  
2600 MH Delft  
The Netherlands

telephone: +31 88 335 82 73  
fax: +31 88 335 85 82  
e-mail: info@deltares.nl  
www: <https://www.deltares.nl>

### **For sales contact:**

telephone: +31 88 335 81 88  
fax: +31 88 335 81 11  
e-mail: software@deltares.nl  
www: <https://www.deltares.nl/software>

### **For support contact:**

telephone: +31 88 335 81 00  
fax: +31 88 335 81 11  
e-mail: software.support@deltares.nl  
www: <https://www.deltares.nl/software>

Copyright © 2019 Deltares

All rights reserved. No part of this document may be reproduced in any form by print, photo print, photo copy, microfilm or any other means, without written permission from the publisher: Deltares.

## Contents

<b>List of Figures</b>	<b>v</b>
<b>List of Tables</b>	<b>vii</b>
<b>1 Introduction</b>	<b>9</b>
<b>2 Momentum advection on rectangular grids</b>	<b>11</b>
2.1 First order upwind (FOU) . . . . .	12
2.2 First order upwind, momentum conservative (FOU-MC-E) . . . . .	13
2.3 First order upwind, with energy-head constancy (FOU-EHC) . . . . .	14
2.4 First order upwind, momentum conservative, cell-based (FOU-MC-C) . . . . .	14
2.5 First order upwind, Stelling & Duinmeijer (FOU-SD) . . . . .	15
2.6 Second-order upwind (SOU) . . . . .	16
2.7 Second order upwind, momentum conservative, edge-based (SOU-MC-E) . . . . .	16
2.8 Second order upwind, momentum conservative, cell-based (SOU-MC-C) . . . . .	17
2.9 Eulerian-Lagrangian scheme . . . . .	17
<b>3 Advection scheme analysis</b>	<b>19</b>
<b>4 Momentum advection on unstructured/irregular grids</b>	<b>21</b>
4.1 TELEMAC . . . . .	21
4.2 D-Flow Flexible Mesh . . . . .	21
4.3 Delft3D . . . . .	22
4.4 UnTRIM . . . . .	23
<b>5 Numerical experiments</b>	<b>25</b>
5.1 Uniform channel flow . . . . .	27
5.2 Flow over a wavy bed . . . . .	28
5.3 Flow over a sloped wavy bed with bottom friction . . . . .	29
5.4 Flow over a sloped wavy bed with emerged groynes . . . . .	29
5.5 Flow over a sloped wavy bed with submerged groynes . . . . .	29
5.6 The Elbe River from Lauenburg to Geesthacht . . . . .	30
<b>6 Results</b>	<b>31</b>
6.1 Uniform channel flow . . . . .	32
6.1.1 Results on rectangular grids . . . . .	32
6.1.2 Results on irregular/unstructured grids . . . . .	32
6.2 Flow over a wavy bed . . . . .	32
6.2.1 Results on rectangular grids . . . . .	33
6.2.2 Results on irregular/unstructured grids . . . . .	35
6.3 Flow over a sloped wavy bed . . . . .	35
6.3.1 Results on rectangular grids . . . . .	36
6.3.2 Results on irregular/unstructured grids . . . . .	37
6.4 Flow over a sloped wavy bed with emerged groynes . . . . .	38
6.4.1 Results on rectangular grids . . . . .	38
6.4.2 Results on irregular/unstructured grids . . . . .	38
6.5 Flow over a sloped wavy bed with submerged groynes . . . . .	39
6.5.1 Results on rectangular grids . . . . .	39
6.5.2 Results on irregular/unstructured grids . . . . .	40
6.6 The Elbe River from Lauenburg to Geesthacht . . . . .	40
6.6.1 Results on rectangular grids . . . . .	40
6.6.2 Results on irregular/unstructured grids . . . . .	41
<b>7 Discussion</b>	<b>51</b>

<b>8 Conclusions</b>	<b>53</b>
8.1 Rectangular discretizations . . . . .	53
8.2 Irregular/unstructured discretizations . . . . .	54
8.3 General conclusions . . . . .	54
<b>9 Outlook</b>	<b>55</b>
<b>10 Final remarks</b>	<b>57</b>
References . . . . .	61

## List of Figures

2.1	The staggered 1D stencil.	12
5.1	Schematic 1D depictions of water level and topography for tests 1–5 . . . . .	26
5.2	Bottom topography for the wavy bed test. . . . .	28
5.3	Bottom topography for the flow over a sloped wavy bed with groynes. . . . .	29
5.4	Digital Terrain Model (DTM) for the Elbe River model. . . . .	30
6.1	Total head loss for the flow over a wavy bed . . . . .	33
6.2	Numerical backwater for the flow over a wavy bed test on irregular/unstructured grids. . . . .	35
6.3	Numerical backwater for the flow over a wavy bed test using UnTRIM . . . . .	36
6.4	Total head loss for the flow over a sloped wavy bed on rectangular grids. . . . .	37
6.5	Numerical backwater for the flow over a sloped wavy bed test on irregular/unstructured grids. . . . .	42
6.6	Momentum terms for the sloped wavy bed. . . . .	42
6.7	Percentual head loss for the flow over a sloped wavy bed with emerged groynes	43
6.8	Vorticity for the flow around emerged groynes. . . . .	43
6.9	Numerical backwater for the flow over a sloped wavy bed with emerged groynes, for the advection schemes from D-Flow FM and Telemac and for the available grid structures, for the $\Delta x \approx 10$ m (top), $\Delta x \approx 5$ m (middle) and $\Delta x \approx 2.5$ m (bottom) resolution grid. . . . .	44
6.10	Artificial head loss for the flow over a sloped wavy bed with submerged groynes on rectangular grids. . . . .	44
6.11	Artificial backwater due to advection for the flow over a sloped wavy bed test with submerged groynes, for all advection schemes and grid structures, for the 10 m (top), 5 m (middle) and 2.5 m (bottom) resolution grid. . . . .	45
6.12	Different acceleration terms in the momentum equation for the sloped channel with groynes, for the longitudinal cross-sections at $y = 75$ m over the groynes (top), $y = 125$ m through the center of the channel, near the groyne tips (middle) and at $y = 175$ m, in main channel (bottom). Note the different vertical scales. . . . .	46
6.13	Percentual artificial head loss due to advection for the Elbe River test case, for the five schematic advection schemes from the analysis and all four grid resolutions. . . . .	47
6.14	Water level in the Elbe River from Lauenburg to Geesthacht using Telemac. . . . .	47
6.15	Water level in the Elbe River from Lauenburg to Geesthacht, comparing Telemac and D-Flow FM. . . . .	47
6.16	Water level in the Elbe River from Lauenburg to Geesthacht. . . . .	48
6.17	Velocities at the mouth of the Elbe Seitenkanal. . . . .	49



## List of Tables

5.1	Topography definitions for the five schematic tests. <sup>a</sup> The maximum Froude number $Fr^{\max} \approx 1$ at the most upstream groyne for the emerged groyne case.	27
6.1	$L_\infty$ norms and convergence rates $p$ for the different advection schemes, for tests 2 and 3 (flow over a wavy bed and over a sloped wavy bed).	34
6.2	Convergence rates for the flow over a sloped wavy bed.	37



## **Contents**



## **List of Figures**



## **List of Tables**



## Summary

The established method for determining dike heights and dimensioning river training structures is to assess the resulting backwater by numerical modelling. The common consensus is that the backwater is dominated by bottom friction and that momentum advection only has a local effect. In this work it is demonstrated that numerical errors in the momentum advection approximation can have an artificial contribution to the backwater which can be of the same order of magnitude as the bottom friction contribution, depending on the chosen advection scheme. This is first realized using a one-dimensional analysis and then verified using one- and two-dimensional numerical experiments.

The geometrical characteristics for the series of test cases were derived from the Elbe River stretch between the German cities Lauenburg and Geesthacht. There, bed forms with an average wave length of approximately 40 m and an amplitude of some 0.3 m were identified. Additionally, groynes are present which are emerged near the banks and submerged near the groyne tips. Therefore, these two geometrical aspects – bed forms and groynes – are the focus of the present work. In the river stretch also bends were present, but these were left out of the present study.

With these considerations, five schematic models with increasing complexity were set up. First, we ran a uniform channel flow test, with a constant slope. Next, we ran a frictionless sinusoidal bed case, with bed form characteristics as described above. Then, these two tests were combined in the third test for the flow along a sloped wavy bed (with bottom friction). These three tests are one-dimensional, but were run using a two-dimensional model. The actual two-dimensional tests consist of the sloped wavy bed test with groynes added to it, both for an emerged and a submerged situation. The final (two-dimensional) test is the river case study itself.

The testing was done in two phases. In the first phase, we performed each test on structured rectangular grids, with 4 different resolutions, with different time steps or maximum (flow) Courant numbers. Here, we tested nine different common advection schemes (six of first-order and three of second-order accuracy). In the second phase, we performed the same tests, on curvilinear and unstructured (triangular) grids, on three different grid resolutions, again with different time steps or maximum (flow) Courant numbers. For this second phase, the numerical modelling systems Telemac, D-Flow Flexible Mesh, Delft3D and UnTRIM were used. In total (phase 1 and 2 together), approximately 600 tests were performed.

In addition to the numerical experiments, a one-dimensional (1D) analysis was performed for three of the nine schematic advection schemes. In this analysis, the artificial backwater due to the advection discretization is quantified. It is demonstrated that a simple first-order upwind advection scheme always has a positive contribution to the backwater, i.e. energy is dissipated when going downstream, causing an additional rise of the upstream water level. For a variant to the first-order upwind scheme, where the advective velocity is chosen slightly different, it can be shown that the contribution to the backwater from the advection term is zero and no additional backwater is generated due to the advection scheme. Finally, for a momentum conservative discretization, it is shown that the backwater cannot be controlled and depends on the local topography. For flow expansions, the scheme dissipates energy and has a positive contribution to the backwater, whereas for flow contractions energy is erroneously gained and the contribution to the backwater is negative.

The common consensus that rivers are dominated by a balance between pressure (or free-surface) gradient and bottom shear stress, is only partly valid. For stationary conditions, with negligible accelerations, this view holds globally. However, already for small accelerations/decelerations, the balance is at least altered locally, due to the advection terms. It

is commonly known that for the flow over sudden topographical variations (e.g. weirs and groynes), such velocity changes are accompanied with energy losses. However, many modellers are unaware of the fact that also small velocity gradients can generate *artificial* energy losses and contribute to this global energy balance, due to inaccuracies in the advection approximation. The size of this contribution was a subject of speculation. In this work, it was demonstrated that the size of the artificial backwater contribution due to the advection approximation is largely determined by the conservation/constancy properties of the scheme and to a lesser extent by the order of the scheme.

## 1 Introduction

In many countries worldwide, costly river engineering projects aim at verifying the dike heights for flood protection or at dimensioning of river training structures (e.g. groynes) for ship navigation and bank protection. In such projects, the backwater needs to be determined with great certainty and accuracy, mostly by one- and two-dimensional numerical modelling.

The backwater arises due to energy losses, commonly assumed to come from bottom friction and turbulent dissipation. However, computer models suffer from numerical errors, which reduce the accuracy of the solution. Such errors mostly originate from the advection approximation for momentum transport, due to its nonlinearity. Here, one might ask: *Do these errors also affect the backwater?*

Most research on the numerical accuracy of advection schemes in shallow-water models is performed using Godunov methods with Riemann solvers, see [Toro and Garcia-Navarro \(2007\)](#) for an overview. These approaches are particularly suited for capturing of shocks or discontinuities, e.g. in dambreak flows or hydraulic jumps. For accurate (quasi-)steady flow predictions over variable topography these schemes require being *well-balanced*, meaning that the flux terms and the source terms need to balance each other in the momentum equations, see e.g. [Noelle et al. \(2007\)](#); [Caleffi and Valiani \(2009\)](#); [Ricchiuto \(2015\)](#); [Caleffi et al. \(2016\)](#) for some recent papers on this topic. These works successfully illustrate the accuracy, conservation and convergence properties of the applied methods using a number of commonly accepted academic test cases for such local phenomena (dambreak, flow over a bump, interacting shocks, etc.). However, many of these applications apply high-resolution grids, where the relevant (topographical) features are sufficiently resolved.

When considering large-scale river applications, with limited grid resolution (with respect to the topography), the local accuracy of the model and the capturing of possible discontinuities is often not feasible and also not the most critical issue. More important is the representation of the total energy loss in the system – resulting in the backwater – and the prediction of areas with increased velocity and bottom shear stress, e.g. for morphodynamic predictions. There may be locations in a model where one might expect energy losses in reality, but where the model lacks the required physical process representation or the resolution to accurately represent the flow patterns causing them, e.g. for the flow over obstacles such as weirs or groynes. For this purpose, the numerical accuracy of the model needs to be investigated differently by focusing on the total flow resistance (physical and numerical).

To the authors' knowledge very few works have considered the numerical errors in this way. [Canestrelli and Toro \(2012\)](#) investigated a FORCE-type centred momentum advection scheme and found that different implementations of the scheme showed considerable differences in the backwater in a river reach, due to numerical diffusion from the advection discretization. This matches the findings of [Stelling and Duinmeijer \(2003\)](#), who examined a number of advection schemes, with different conservation/constancy properties, and showed how the head loss varies for the flow over sudden expansions, contractions and over a weir.

In this work, we continue these considerations and provide a new interpretation of discretization errors in numerical river modelling, introducing the concept of *numerical* or *artificial backwater*. We focus on real-world, quasi-steady river applications with complex geometry and the use of feasible grid resolution for engineering practice. The aim of this work is to determine whether there is an artificial contribution to the backwater from the momentum advection approximation, for river applications with variable topography. We determine the contribution to the global backwater from errors in the advection scheme through an analysis of the steady inviscid momentum equation, also called the backwater or Bélanger equation, see e.g. [Chanson \(2004, 2009\)](#).

The results from this analysis are then confirmed using a sequence of tests with flow over variable topography. A set of test problems was defined that increases in complexity towards a real-world case study of a 17 km stretch of the Elbe river in Germany.

The work is split in two parts. First, we consider discretizations on rectangular grids, where we analyze the discretizations of several common first- and second-order accurate advection schemes for their contribution to the backwater, applying the vertically integrated, two-dimensional model from [Platzek et al. \(2016\)](#). In this part, the effect of the grid structure is absent and we analyze the effect of the advection scheme, exclusively. In the second part of this work, we switch to curvilinear and triangular grids, to investigate the combined effect of the grid structure and the advection scheme, for several well-tested numerical modelling systems developed for shallow-water applications.

In section 2, we introduce the discretizations for momentum advection on rectangular grids, for which we analyze the artificial backwater contributions using a 1D analysis in section 3. Next, in section 4, we briefly introduce the modelling systems that we tested on curvilinear and triangular grids. We describe the series of test cases in section 5, for which we present the results in section 6. We end with a discussion and conclusions in sections 7 and 8.

## 2 Momentum advection on rectangular grids

The modelling systems used for real-world river applications are often based on (semi-)implicit, staggered grid, finite-difference methods: e.g. POM (Blumberg and Mellor (1987)), UnTRIM (Casulli and Walters (2000)), Suntans (Fringer *et al.* (2006)), Delft3D (Deltares (2013)), MIKE 21 (DHI (2011)) and HEC-RAS (Brunner (2016)). Due to the implicit treatment of the pressure terms, the Courant number for stability is only based on the flow velocity  $u$  and not on the wave celerity  $c = \sqrt{gH}$ . For this reason – for low-Froude number, quasi-steady river computations – these approaches allow the application of relatively large time steps and suffer from numerical diffusion that only scales with  $u$  and not with  $u \pm c$ .

The (nonlinear) momentum advection schemes in the aforementioned models are often extensions/combinations of several basic upwind schemes. In this section, we present a number of such schemes, which have been chosen for their different properties and complexities. The schemes have been implemented and tested in a two-dimensional, depth-averaged shallow-water solver (Platzek *et al.* (2016)). For the present investigations, the contributions due to horizontal diffusion, Coriolis and wind are neglected. The momentum and continuity equations then read:

$$\frac{\partial u}{\partial t} + u \frac{\partial u}{\partial x} + v \frac{\partial u}{\partial y} + g \frac{\partial \zeta}{\partial x} + \frac{\gamma |U| u}{H} = 0 \quad (2.1)$$

$$\frac{\partial v}{\partial t} + u \frac{\partial v}{\partial x} + v \frac{\partial v}{\partial y} + g \frac{\partial \zeta}{\partial y} + \frac{\gamma |U| v}{H} = 0 \quad (2.2)$$

$$\frac{\partial \zeta}{\partial t} + \frac{\partial (Hu)}{\partial x} + \frac{\partial (Hv)}{\partial y} = 0 \quad (2.3)$$

where  $u$  and  $v$  are the depth-averaged velocities in the  $x$ - and  $y$ -directions;  $\zeta$  is the free-surface position;  $H$  is the total water depth defined as  $H = \zeta - h$ , where  $h$  is the bed level;  $t$  represents time;  $g$  is the gravitational acceleration and  $\gamma$  is the bottom friction coefficient, computed using e.g. a Chézy, Manning or Nikuradse roughness formulation and  $|U| = (u^2 + v^2)^{1/2}$ .

The equations are discretized on a uniform Cartesian grid, with grid sizes  $\Delta x$  and  $\Delta y$ . The grid has  $I$  cells in the  $x$ -direction and  $J$  cells in the  $y$ -direction. We use a C-grid administration (staggered positioning of variables), i.e. the water level  $\zeta$  is specified in cell centres and the velocity components  $u$  and  $v$  at cell edges (see Fig. 2.1 for a 1D representation).  $\Omega_{i,j}$  is the cell at position  $(i, j)$ , where  $i$  and  $j$  are the indices in  $x$  and  $y$ -direction, respectively, with  $i = 1, 2, \dots, I$ ;  $j = 1, 2, \dots, J$ . We discretize the momentum equation ((2.1)) for each cell edge  $\Gamma_{i+1/2,j}$  using a semi-implicit time discretization where the advection term is treated explicitly and both the free-surface gradient and the bottom friction term are discretized implicitly (see e.g. Casulli (1990); Casulli and Cattani (1994)):

$$\frac{u_{i+1/2,j}^{n+1} - u_{i+1/2,j}^n}{\Delta t^n} + F u_{i+1/2,j}^n + g \frac{\zeta_{i+1,j}^{n+1} - \zeta_{i,j}^{n+1}}{\Delta x} + \frac{\gamma_{i+1/2,j}^n}{H_{i+1/2,j}^n} |U_{i+1/2,j}^n| u_{i+1/2,j}^{n+1} = 0 \quad (2.4)$$

where  $n$  is the time level and  $\Delta t^n$  is the time step size at level  $n$ . The operator  $F u_{i+1/2,j}^n$  contains the explicit discretization of the momentum advection term and is the subject of the present investigation. The momentum equation in the  $y$ -direction ((2.2)) is discretized similarly.

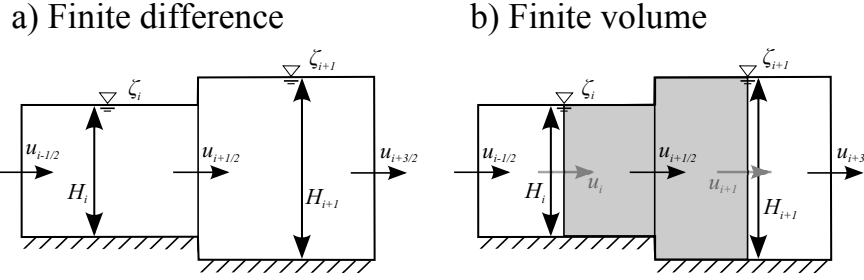


**Figure 2.1:** The staggered 1D stencil with water level  $\zeta$  and total depth  $H$  in the cell centres and velocity  $u$  and at the edges. a): the finite difference stencil. b): the finite volume stencil with the velocity volume (grey area) and the cell centre velocities  $u_i$  (grey vectors).

We investigate the effect on the backwater of different basic discretizations for the advective operator  $Fu$  (and  $Fv$ ). The following nine schemes are considered:

- |   |  |            |
|---|--|------------|
| 1 | First-order upwind   | (FOU)      |
| 2 | First-order upwind, momentum conservative, edge based              | (FOU-MC-E) |
| 3 | First-order upwind, with energy-head constancy                     | (FOU-EHC)  |
| 4 | First-order upwind, momentum conservative, cell-based              | (FOU-MC-C) |
| 5 | First-order upwind, <a href="#">Stelling and Duinmeijer (2003)</a> | (FOU-SD)   |
| 6 | Second-order upwind  | (SOU)      |
| 7 | Second-order upwind, momentum conservative, edge-based             | (SOU-MC-E) |
| 8 | Second-order upwind, momentum conservative, cell-based             | (SOU-MC-C) |
| 9 | Eulerian-Lagrangian  | (EL)       |

and for the first three we perform an analysis of the contribution to the backwater.

For brevity, only the discretization of the longitudinal advection term  $u\partial u/\partial x$  as in a 1D model (leaving out the cross-advection term  $v\partial u/\partial y$ ) is presented. Similar expressions hold for the discretization of  $Fv$  in two dimensions. The first three schemes – for which we perform the analysis in Section 3 – can be written in the following general form:

$$Fu_{i+1/2,j}^n = u_{i+1,j}^+ \frac{u_{i+3/2,j}^n - u_{i+1/2,j}^n}{\Delta x} + u_{i,j}^- \frac{u_{i+1/2,j}^n - u_{i-1/2,j}^n}{\Delta x} \quad (2.5)$$

The definitions of the advective velocities  $u_{i+1,j}^+$  and  $u_{i,j}^-$  determine the properties of the scheme.

## 2.1 First order upwind (FOU)

This is the simplest upwind discretization. The advection term is computed using ((2.5)), where the advective velocities are simply taken first-order upwind:

$$u_{i+1,j}^+ = \begin{cases} 0 & \text{if } u_{i+1/2,j}^n \geq 0 \\ u_{i+1/2,j}^n & \text{if } u_{i+1/2,j}^n < 0 \end{cases} \quad (2.6)$$

$$u_{i,j}^- = \begin{cases} u_{i+1/2,j}^n & \text{if } u_{i+1/2,j}^n > 0 \\ 0 & \text{if } u_{i+1/2,j}^n \leq 0 \end{cases} \quad (2.7)$$

For positive flow direction ( $u_{i+1/2,j} > 0$ ), insertion of these advective velocities in ((2.5)) results in:

$$Fu_{i+1/2,j}^n = u_{i+1/2,j}^n \frac{u_{i+1/2,j}^n - u_{i-1/2,j}^n}{\Delta x} \quad (2.8)$$

## 2.2 First order upwind, momentum conservative (FOU-MC-E)

In this discretization, that was introduced in [Stelling and Duinmeijer \(2003\)](#), a conservative finite volume formulation is rewritten to a simple finite difference method with the same properties. The method was extended to unstructured grids based on the work by [Perot \(2000\)](#) in [Kramer and Stelling \(2008\)](#) and applied and further developed in [Kernkamp et al. \(2011\)](#); [Kleptsova et al. \(2012\)](#). It was applied in combination with high-resolution subgrid topography by [Stelling \(2012\)](#) (on quadtree grids) and [Volp et al. \(2013\)](#). With the chosen semi-implicit temporal discretization, it can only be demonstrated to be momentum conservative on a discrete level for stationary conditions. It is derived by rewriting the advection term from [\(2.1\)](#)) into:

$$u \frac{\partial u}{\partial x} = \frac{1}{H} \left( \frac{\partial (qu)}{\partial x} - u \frac{\partial q}{\partial x} \right) \quad (2.9)$$

where  $q = hu$  is the specific discharge. Discretizing for edge  $\Gamma_{i+1/2,j}$  at time level  $n$ , we get:

$$Fu_{i+1/2,j}^n = \frac{1}{\bar{H}_{i+1/2,j}^n} \left( \frac{\bar{q}_{i+1,j}^x u_{i+1,j}^* - \bar{q}_{i,j}^x u_{i,j}^*}{\Delta x} - u_{i+1/2,j} \frac{\bar{q}_{i+1,j}^x - \bar{q}_{i,j}^x}{\Delta x} \right) \quad (2.10)$$

where

$$\begin{aligned} \bar{q}_{i,j}^x &= \frac{1}{2} (q_{i-1/2,j}^x + q_{i+1/2,j}^x) \\ &= \frac{1}{2} (H_{i-1/2,j}^* u_{i-1/2,j}^n + H_{i+1/2,j}^* u_{i+1/2,j}^n) \end{aligned} \quad (2.11)$$

$$\bar{H}_{i+1/2,j}^n = \frac{1}{2} (H_{i,j}^n + H_{i+1,j}^n) \quad (2.12)$$

$$H_{i+1/2,j}^* = \begin{cases} \zeta_{i,j}^n + h_{i+1/2,j}^n & \text{if } u_{i+1/2,j}^n \geq 0 \\ \zeta_{i+1,j}^n + h_{i+1/2,j}^n & \text{if } u_{i+1/2,j}^n < 0 \end{cases} \quad (2.13)$$

$$u_{i,j}^* = \begin{cases} u_{i-1/2,j}^n & \text{if } u_{i-1/2,j}^n + u_{i+1/2,j}^n \geq 0 \\ u_{i+1/2,j}^n & \text{if } u_{i-1/2,j}^n + u_{i+1/2,j}^n < 0 \end{cases} \quad (2.14)$$

For flow in the positive  $x$ -direction, this simplifies to the following advection term:

$$u \frac{\partial u}{\partial x} \Big|_{i+1/2}^n = \frac{q_{i-1/2,j}^x + q_{i+1/2,j}^x}{H_{i,j}^n + H_{i+1,j}^n} \frac{u_{i+1/2,j}^n - u_{i-1/2,j}^n}{\Delta x} \quad (2.15)$$

The advective velocities in [\(2.5\)](#)) for this scheme are thus computed as:

$$u_{i+1,j}^+ = \begin{cases} 0 & \text{if } u_{i+1/2,j}^n + u_{i+3/2,j}^n \geq 0 \\ \frac{q_{i+1/2,j}^x + q_{i+3/2,j}^x}{H_{i,j}^n + H_{i+1,j}^n} & \text{if } u_{i+1/2,j}^n + u_{i+3/2,j}^n < 0 \end{cases} \quad (2.16)$$

$$u_{i,j}^- = \begin{cases} \frac{q_{i-1/2,j}^x + q_{i+1/2,j}^x}{H_{i,j}^n + H_{i+1,j}^n} & \text{if } u_{i-1/2,j}^n + u_{i+1/2,j}^n \geq 0 \\ 0 & \text{if } u_{i-1/2,j}^n + u_{i+1/2,j}^n < 0 \end{cases} \quad (2.17)$$

where  $q_{i+1/2,j}^x = Q_{i+1/2,j}^n / \Delta y$  is the specific discharge in  $x$ -direction. The detailed derivation can be found in [Stelling and Duinmeijer \(2003\)](#).

### 2.3 First order upwind, with energy-head constancy (FOU-EHC)

This discretization was also introduced in [Stelling and Duinmeijer \(2003\)](#) and applied in [Kramer and Stelling \(2008\)](#); [Platzek et al. \(2016\)](#). The advection is again expressed as ((2.5)), and the advective velocities are computed as:

$$u_{i+1,j}^+ = \begin{cases} 0 & \text{if } u_{i+1/2,j}^n + u_{i+3/2,j}^n \geq 0 \\ -\frac{1}{2} (u_{i+1/2,j}^n + u_{i+3/2,j}^n) & \text{if } u_{i+1/2,j}^n + u_{i+3/2,j}^n < 0 \end{cases} \quad (2.18)$$

$$u_{i,j}^- = \begin{cases} \frac{1}{2} (u_{i-1/2,j}^n + u_{i+1/2,j}^n) & \text{if } u_{i-1/2,j}^n + u_{i+1/2,j}^n \geq 0 \\ 0 & \text{if } u_{i-1/2,j}^n + u_{i+1/2,j}^n < 0 \end{cases} \quad (2.19)$$

For positive flow direction ( $u_{i+1/2} > 0$ ), insertion of these advective velocities in ((2.5)) results in:

$$\begin{aligned} F u_{i+1/2,j}^n &= \frac{u_{i-1/2,j}^n + u_{i+1/2,j}^n}{2} \frac{u_{i+1/2,j}^n - u_{i-1/2,j}^n}{\Delta x} \\ &= \frac{\frac{1}{2} (u_{i+1/2,j}^n)^2 - \frac{1}{2} (u_{i-1/2,j}^n)^2}{\Delta x} \end{aligned} \quad (2.20)$$

Combined with a central discretization of the pressure gradient, this scheme keeps the energy head  $\zeta_{i,j} + u_{i-1/2,j}^2/(2g)$  (note the shifted indices) constant along streamlines without introducing any backwater. The analysis in section 3 and the numerical tests in section 5 confirm this property.

### 2.4 First order upwind, momentum conservative, cell-based (FOU-MC-C)

This discretization is based on the scheme developed for the Navier-Stokes equations by [Perot \(2000\)](#) and was presented for the 2D Shallow Water equations in [Kramer and Stelling \(2008\)](#). It can be seen as a generalization of the momentum conservative scheme from [Stelling and Duinmeijer \(2003\)](#) (section 2.2) to unstructured grids. As with the scheme from section 2.2, it can only be demonstrated to be momentum conservative on a discrete level for stationary solutions. The scheme is also applied in [Kernkamp et al. \(2011\)](#) and in a slightly modified form and in 3D in [Kleptsova et al. \(2010, 2012\)](#). It is based on the same principles as the scheme from Section 2.2, but instead of it being defined directly for the advection term on a cell edge, first a cell-based advection term is computed (the full advection vector), which is then mapped to the edges of the cell using appropriate weighting, based on distance, water depth or volume, determining the variants of the scheme.

We have chosen the following implementation of the scheme (for comparison and details of the derivation see [Kramer and Stelling \(2008\)](#); [Kleptsova et al. \(2010\)](#); [Kernkamp et al. \(2011\)](#); [Kleptsova et al. \(2012\)](#)). Again it starts by rewriting the advection term in a similar way as in Section 2.2:

$$u \frac{\partial u}{\partial x} = \frac{1}{A^x} \left( \frac{\partial (Qu)}{\partial x} - u \frac{\partial Q}{\partial x} \right) \quad (2.21)$$

But now this term is discretized using a finite volume approach as a weighted sum of contributions from the two adjacent cells of the face. On a rectangular grid, this weighting becomes

a simple average. For edge  $\Gamma_{i+1/2,j}$  at time level  $n$ , we get:

$$u \frac{\partial u}{\partial x} \Big|_{i+1/2,j}^n = \frac{1}{\bar{V}_{i+1/2,j}^n} \left\{ \frac{1}{2} (Q_{i+3/2,j}^x u_{i+3/2,j}^* - Q_{i+1/2,j}^x u_{i+1/2,j}^*) \right. \quad (2.22)$$

$$\begin{aligned} & - \frac{1}{2} \bar{u}_{i+1,j} (Q_{i+3/2,j}^x - Q_{i+1/2,j}^x) \\ & + \frac{1}{2} (Q_{i+1/2,j}^x u_{i+1/2,j}^* - Q_{i-1/2,j}^x u_{i-1/2,j}^*) \end{aligned} \quad (2.23)$$

$$- \frac{1}{2} \bar{u}_{i,j} (Q_{i+1/2,j}^x - Q_{i-1/2,j}^x) \} \quad (2.24)$$

where

$$Q_{i+1/2,j}^x = \Delta y H_{i+1/2,j}^n u_{i+1/2,j}^n \quad (2.25)$$

$$\bar{V}_{i+1/2,j}^n = \frac{1}{2} (V_{i,j}^n + V_{i+1,j}^n) \quad (2.26)$$

$$H_{i+1/2,j}^n = \begin{cases} \zeta_{i,j}^n + h_{i+1/2,j}^n & \text{if } u_{i+1/2,j}^n \geq 0 \\ \zeta_{i+1,j}^n + h_{i+1/2,j}^n & \text{if } u_{i+1/2,j}^n < 0 \end{cases} \quad (2.27)$$

$$u_{i+1/2,j}^* = \begin{cases} \bar{u}_{i,j}^n & \text{if } u_{i+1/2,j}^n \geq 0 \\ \bar{u}_{i+1,j}^n & \text{if } u_{i+1/2,j}^n < 0 \end{cases} \quad (2.28)$$

$$\bar{u}_{i,j} = \frac{1}{2} (u_{i-1/2,j}^n + u_{i+1/2,j}^n) \quad \text{Perot's weighting for uniform} \\ \text{structured grids} \quad (2.29)$$

This scheme can not be written in the general form ((2.5)). Assuming positive flow direction, a number of terms will cancel, but the scheme will be of a different form. Two important differences to the scheme from section 2.2 can be noticed. First, the stencil of the scheme covers two full cells instead of two half cells, thereby using the velocities from more faces. Second, the scheme involves averaging of velocities  $u$  (in  $\bar{u}_{i,j}$ ) instead of averaging of  $Q$ . Considering the fact that in many flow situations, the discharge  $Q$  will show much less variation than  $u$  (due to continuity), this may be a negative aspect of this scheme.

## 2.5 First order upwind, Stelling & Duinmeijer (FOU-SD)

This discretization that was also introduced in [Stelling and Duinmeijer \(2003\)](#) switches between momentum conservation and constancy of energy head. It was generalized to unstructured grids in [Kramer and Stelling \(2008\)](#). It aims to deal with the fact that our differential and non-conservative form of the shallow water equations is not valid for situations with discontinuous solutions, where streamlines are strongly curved, as e.g. for the flow over a weir or through a sudden contraction. In such a situation, the hydrostatic pressure assumption is not valid and applying strict momentum conservation would then lead to an increase in energy head ([Stelling and Duinmeijer \(2003\)](#); [Kramer and Stelling \(2008\)](#)). In such contractions – to avoid physically unrealistic solutions – it is better to apply a formulation that maintains a constant energy head.

For this purpose, in the scheme from [Stelling and Duinmeijer \(2003\)](#); [Kramer and Stelling \(2008\)](#), the advective velocities are based on an algorithm that switches between momentum conservation and energy-head constancy at expansions and contractions, respectively. For contractions, i.e. if  $\frac{u_{i+1/2,j}^n - u_{i-1/2,j}^n}{\Delta x} > \epsilon > 0$  ([Stelling and Duinmeijer \(2003\)](#)), the upwind velocities providing energy-head constancy are applied, using ((2.18))-(2.19)). Otherwise,

i.e. if  $\frac{u_{i+1/2,j}^n - u_{i-1/2,j}^n}{\Delta x} \leq \epsilon$ , the upwind velocities giving momentum conservation ((2.16))-((2.17)) are used. Here  $\epsilon$  is a threshold value which can be chosen such that the scheme with energy constancy is only applied in strong contractions, where the hydrostatic pressure assumption is not valid and momentum conservation yields erroneous results.

## 2.6 Second-order upwind (SOU)

This scheme is the extension of the first order upwind scheme in Section 2.1, based on inclusion of an extra term from the Taylor series expansion. It can not be written in the general form of the first-order schemes ((2.5)). Instead the discretization reads:

$$Fu_{i+1/2,j}^n = -\frac{1}{\Delta x} [u_{i+1,j}^* (u_{i+5/2,j}^n - 4u_{i+3/2,j}^n + 3u_{i+1/2,j}^n) + u_{i,j}^* (3u_{i+1/2,j}^n - 4u_{i-1/2,j}^n + u_{i-3/2,j}^n)] \quad (2.30)$$

with advective velocities  $u_{i+1}^*$  and  $u_i^*$ :

$$u_{i+1,j}^* = \begin{cases} 0 & \text{if } u_{i+1/2,j}^n \geq 0 \\ u_{i+1/2,j}^n & \text{if } u_{i+1/2,j}^n < 0 \end{cases} \quad (2.31)$$

$$u_{i,j}^* = \begin{cases} u_{i+1/2,j}^x & \text{if } u_{i+1/2,j}^n \geq 0 \\ 0 & \text{if } u_{i+1/2,j}^n < 0 \end{cases} \quad (2.32)$$

This scheme can be shown to be second-order accurate in space on a regular grid.

## 2.7 Second order upwind, momentum conservative, edge-based (SOU-MC-E)

The scheme from section 2.2 can be improved by using second-order accurate interpolation with a slope limiter (see e.g. Stelling and Duinmeijer (2003)), to compute both the upwind value for  $u_{i,j}^*$  at the cell centre and the water level  $\zeta_{i+1/2,j}^*$  needed at the cell face to compute the total depth  $H_{i+1/2}$ . In practice, the slope limiter makes sure that the scheme reduces to first order when there is large local variation of the gradients. In the end, only the computation of the upwind expressions for  $H_{i+1/2,j}^n$  and for  $u_{i,j}^*$  is modified:

$$H_{i+1/2,j}^n = \zeta_{i+1/2,j}^* + h_{i+1/2,j}^n \quad (2.33)$$

$$\zeta_{i+1/2,j}^* = \begin{cases} \zeta_{i,j}^n + \frac{1}{2}\psi(r_+^\zeta)(\zeta_{i,j}^n - \zeta_{i-1,j}^n) & \text{if } u_{i+1/2,j}^n \geq 0 \\ \zeta_{i+1,j}^n - \frac{1}{2}\psi(r_-^\zeta)(\zeta_{i+2,j}^n - \zeta_{i+1,j}^n) & \text{if } u_{i+1/2,j}^n < 0 \end{cases} \quad (2.34)$$

$$r_+^\zeta = \frac{\zeta_{i+1,j}^n - \zeta_{i,j}^n}{\zeta_{i,j}^n - \zeta_{i-1,j}^n}, \quad r_-^\zeta = \frac{\zeta_{i+1,j}^n - \zeta_{i,j}^n}{\zeta_{i+2,j}^n - \zeta_{i+1,j}^n} \quad (2.35)$$

$$u_{i,j}^* = \begin{cases} u_{i-1/2,j}^n + \frac{1}{2}\psi(r_+^u)(u_{i-1/2,j}^n - u_{i-3/2,j}^n) & \text{if } u_{i-1/2,j}^n + u_{i+1/2,j}^n \geq 0 \\ u_{i+1/2,j}^n - \frac{1}{2}\psi(r_-^u)(u_{i+3/2,j}^n - u_{i+1/2,j}^n) & \text{if } u_{i-1/2,j}^n + u_{i+1/2,j}^n < 0 \end{cases} \quad (2.36)$$

$$r_+^u = \frac{u_{i+1,j}^n - u_{i,j}^n}{u_{i,j}^n - u_{i-1,j}^n}, \quad r_-^u = \frac{u_{i+1,j}^n - u_{i,j}^n}{u_{i+2,j}^n - u_{i+1,j}^n} \quad (2.37)$$

For the evaluation of the limiter function  $\psi$  many variants are known from the literature, see e.g. Zhang *et al.* (2015). We have implemented and tested several (MinMod, Van Leer, Koren, Monotomized Central, etc.), but the MinMod limiter showed the least restriction on the time step for stability and is applied in the present work:

$$\psi(r^u) = \max(0, \min(1, r^u)) \quad (2.38)$$

For the water levels  $\zeta$  the expression is defined accordingly.

## 2.8 Second order upwind, momentum conservative, cell-based (SOU-MC-C)

A similar second-order extension can be made to the scheme from section 2.4. The scheme is derived in a similar way as the second order extension of section 2.7. The difference is that all expressions are shifted by half a cell due to the fact that the discretizations are set up in the cell centres instead of on the edges.

## 2.9 Eulerian-Lagrangian scheme

Eulerian-Lagrangian schemes are set up differently than the previous schemes. For an Eulerian-Lagrangian advection scheme (see e.g. Casulli and Cheng (1990); Staniforth and Côté (1991); Ham *et al.* (2006)), the total derivative of the velocity  $Du/Dt$  is discretized directly instead of discretizing the time derivative of the velocity and the advection term separately. In 1D this looks as follows:

$$\frac{Du}{Dt} = \frac{\partial u}{\partial t} + u \frac{\partial u}{\partial x} \quad (2.39)$$

And discretizing the total derivative we get:

$$\left. \frac{Du}{Dt} \right|_{i+1/2} = \frac{u_{i+1/2}^{n+1} - u_a^n}{\Delta t} \quad (2.40)$$

where  $a$  is the foot of the Lagrangian trajectory, found by tracking back for one time step  $\Delta t$  from point  $x_{i+1/2}$ , where the velocity  $u_a^n$  commonly has to be found by interpolation between grid values of the velocity. When the local Courant number  $C_{i+1/2} = u_{i+1/2} \Delta t / \Delta x \leq 1$ , a simple first-order approximation is to interpolate between  $u_{i-1/2}$  and  $u_{i+1/2}$  as follows:

$$u_a^n = C_{i+1/2} u_{i-1/2}^n + (1 - C_{i+1/2}) u_{i+1/2}^n \quad (2.41)$$

The discretization of the total derivative ((2.40)) then becomes:

$$\left. \frac{Du}{Dt} \right|_{i+1/2} = \frac{u_{i+1/2}^{n+1} - u_a^n}{\Delta t} = \frac{u_{i+1/2}^{n+1} - u_{i+1/2}^n}{\Delta t} + u_{i+1/2}^n \frac{u_{i+1/2}^n - u_{i-1/2}^n}{\Delta x} \quad (2.42)$$

which is identical to the first order upwind discretization using (2.7).

For a local Courant number  $C_{i+1/2} > 1$ , the discretization becomes of a different nature. For instance, for  $1 < C_{i+1/2} < 2$  (and  $u_{i+1/2}^n > 0 \forall i$ ), the foot of the trajectory lies in cell  $i - 1$ . We travel a distance  $\Delta x$  in time  $\Delta t' = \Delta x / u_{i+1/2}^n$  in cell  $i$  and we are left with a distance  $\Delta s = u_{i-1/2}^n \tilde{\Delta t}$ , with  $\tilde{\Delta t} = \Delta t - \Delta t'$  to be travelled in cell  $i - 1$ , with modified local Courant number:

$$\begin{aligned} \tilde{C}_{i-1/2} &= \frac{u_{i-1/2}^n \tilde{\Delta t}}{\Delta x} = \frac{u_{i-1/2}^n \left( \Delta t - \frac{\Delta x}{u_{i+1/2}^n} \right)}{\Delta x} \\ &= \frac{u_{i-1/2}^n \Delta t}{\Delta x} - \frac{u_{i-1/2}^n}{u_{i+1/2}^n} \end{aligned} \quad (2.43)$$

The velocity at the foot of the trajectory  $u_a$  becomes:

$$\begin{aligned}
 u_a^n &= \tilde{C}_{i-1/2} u_{i-3/2}^n + \left(1 - \tilde{C}_{i-1/2}\right) u_{i-1/2}^n \\
 &= \left(\frac{u_{i-1/2}^n \Delta t}{\Delta x} - \frac{u_{i-1/2}^n}{u_{i+1/2}^n}\right) u_{i-3/2}^n - \left(1 - \frac{u_{i-1/2}^n \Delta t}{\Delta x} + \frac{u_{i-1/2}^n}{u_{i+1/2}^n}\right) u_{i-1/2}^n \\
 &= u_{i-1/2}^n - \Delta t u_{i-1/2}^n \frac{u_{i-1/2}^n - u_{i-3/2}^n}{\Delta x} + \frac{u_{i-1/2}^n}{u_{i+1/2}^n} (u_{i-1/2}^n - u_{i-3/2}^n) \quad (2.44)
 \end{aligned}$$

Substituting ((2.44)) in ((2.40)), we obtain:

$$\begin{aligned}
 \frac{Du}{Dt} \Big|_{i+1/2} &= \frac{u_{i+1/2}^{n+1} - u_{i-1/2}^n}{\Delta t} + u_{i-1/2}^n \frac{u_{i-1/2}^n - u_{i-3/2}^n}{\Delta x} \\
 &\quad - \frac{u_{i-1/2}^n}{u_{i+1/2}^n} \frac{u_{i-1/2}^n - u_{i-3/2}^n}{\Delta t} \quad (2.45)
 \end{aligned}$$

It can be demonstrated that such relations are built recursively, for increasing values of the Courant number, e.g. for  $2 < C_{i+1/2} \leq 3$  one obtains:

$$\begin{aligned}
 \frac{Du}{Dt} \Big|_{i+1/2} &= \frac{u_{i+1/2}^{n+1} - u_{i-3/2}^n}{\Delta t} + u_{i-3/2}^n \frac{u_{i-3/2}^n - u_{i-5/2}^n}{\Delta x} \\
 &\quad - \frac{u_{i-1/2}^n}{u_{i+1/2}^n} \frac{u_{i-1/2}^n - u_{i-3/2}^n}{\Delta t} - \frac{u_{i-3/2}^n}{u_{i+1/2}^n} \frac{u_{i-3/2}^n - u_{i-5/2}^n}{\Delta t} \quad (2.46)
 \end{aligned}$$

Instead of taking the local Courant number  $C_{i+1/2} = u_{i+1/2} \Delta t / \Delta x$  and using that to interpolate the velocity at the foot of the trajectory, we perform sub-time-stepping with a local Courant number of  $C = 0.1$ , and bi-linearly interpolate the velocity to the point along the track. For such a recursive relation the considerations made above can be performed, but they render a tedious and lengthy process, with corresponding recursive relations for the equivalent finite difference formulation. From numerical experiments it was found that for Courant numbers between 0 and 1, the Eulerian-Lagrangian has numerical head losses somewhere between the FOU and the FOU-EHC scheme, depending on the chosen interpolation type. As can be seen from the equations above, the discrete advection operator depends on the chosen time step  $\Delta t$  (or the Courant number  $C$ ). Therefore, it can be expected that the steady-state solution for computations employing the Eulerian-Lagrangian scheme will also depend on the chosen  $\Delta t$  or  $C$ . This is, of course, undesirable. Additionally, for larger Courant numbers the solutions behave differently and may show spurious modes due to the additional terms that appear in Eqs. ((2.44)) and ((2.46)).

### 3 Advection scheme analysis

We now analyse the momentum equation ((2.4)) and determine the artificial contribution to the backwater due to the advection approximation. For simplicity, we only analyse the three first-order accurate schemes from section 2. We restrict ourselves to steady, inviscid, 1D flow and consider only flow in the positive direction ( $u > 0$ ).

The FOU and FOU-EHC scheme are strict finite difference schemes, whereas the FOU-MC-E scheme is derived from a finite volume scheme (see also Fig. 2.1). For the purpose of performing a general analysis for the three schemes, we define left (L) and right (R) velocities as follows:

$$\begin{aligned} \text{FOU / FOU-EHC : } & u_L = u_{i-1/2}, & u_R = u_{i+1/2} \\ \text{FOU-MC-E : } & u_L = u_i, & u_R = u_{i+1} \end{aligned} \quad (3.1)$$

where we leave the actual definition of the cell centre velocities  $u_i$  and  $u_{i+1}$  open. The water levels for all three schemes are defined as  $\zeta_L = \zeta_i$  and  $\zeta_R = \zeta_{i+1}$ . In this way, the schemes can be written in a general form and ((2.4)) reduces to (dropping the time level  $n$  since we have assumed a steady state):

$$(\alpha u_L + (1 - \alpha) u_R) \frac{u_R - u_L}{\Delta x} + g \frac{\zeta_R - \zeta_L}{\Delta x} = 0 \quad (3.2)$$

with coefficient  $\alpha$ :

$$\begin{aligned} \text{FOU : } & \alpha = 0 \\ \text{FOU-EHC : } & \alpha = \frac{1}{2} \\ \text{FOU-MC-E : } & \alpha = u_R / (u_L + u_R) \end{aligned} \quad (3.3)$$

where the expression for  $\alpha$  for the FOU-MC-E scheme was obtained using  $q = Hu$ , providing  $\alpha = H_L / (H_L + H_R) = u_R / (u_L + u_R)$ .

We now integrate the momentum equation over all cells in the  $x$ -direction and scale with  $g$  to obtain an expression with the dimension of the energy head ([m]):

$$M = \frac{\Delta x}{g} \sum_{i=1}^I \left\{ (\alpha u_L + (1 - \alpha) u_R) \frac{u_R - u_L}{\Delta x} + g \frac{\zeta_R - \zeta_L}{\Delta x} \right\} \quad (3.4)$$

which can be rewritten as  $M = \Delta H + \Delta H^{ADV}$  (where ADV denotes the chosen advection scheme), to give the backwater  $\Delta H$  in terms of the energy head  $\zeta + u^2 / (2g)$ :

$$\begin{aligned} M &= \frac{1}{g} \sum_{i=1}^I \left\{ \left( g\zeta_L + \frac{1}{2}u_L^2 \right) - \left( g\zeta_R + \frac{1}{2}u_R^2 \right) \right\} \\ &+ \frac{1}{g} \sum_{i=1}^I \left\{ \left( \frac{1}{2} - \alpha \right) u_L^2 + \left( \frac{1}{2} - \alpha \right) u_R^2 + (2\alpha - 1) u_L u_R \right\} \end{aligned} \quad (3.5)$$

where the first term on the right is a conservative discretization of the gradient of the energy head which does not contribute to the backwater. The term on the second line forms the backwater contribution from the advection term. We can inspect its value for different values of  $\alpha$ . It can easily be seen that for the energy-head constancy scheme FOU-EHC (with  $\alpha = 1/2$ ), the total head loss is zero:  $\Delta H^{ADV} = \Delta H^{FOU-EHC} = 0$  and the advection term has no contribution to the backwater, as was expected for this scheme.

For  $\alpha = 0$  (the FOU scheme), the backwater contribution  $\Delta H$  becomes:

$$\begin{aligned}\Delta H^{FOU} &= \frac{1}{g} \sum_{i=1}^I \left\{ \frac{1}{2} u_L^2 + \frac{1}{2} u_R^2 - u_L u_R \right\} \\ &= \frac{1}{2g} \sum_{i=1}^I (u_L - u_R)^2\end{aligned}\quad (3.6)$$

which is identical to the sum of all Carnot losses over the channel (without contraction/expansion coefficient), see e.g. [Chanson \(2004\)](#). This term is quadratic and therefore, the backwater contribution from advection for the FOU scheme is always positive.

The same analysis can be done for the FOU-MC-E scheme. Inserting  $\alpha$  from ((3.3)) in ((3.5)) and rearranging, we obtain:

$$\Delta H^{FOU-MC-E} = \frac{1}{2g} \sum_{i=1}^I \frac{(u_L - u_R)^3}{u_L + u_R} \quad (3.7)$$

We can compare the sign and size of ((3.7)) and ((3.6)) by computing the ratio between the local artificial head loss for the FOU-MC-E and FOU scheme:

$$r_{i+1/2} = \frac{\Delta H_{i+1/2}^{FOU-MC-E}}{\Delta H_{i+1/2}^{FOU}} = \frac{u_L - u_R}{u_L + u_R} \quad (3.8)$$

Since we assumed positive flow direction, this ratio is always smaller than 1 and therefore the backwater from the FOU-MC-E scheme is always less than that from the FOU scheme. Moreover, the ratio is positive for  $u_L > u_R$ , i.e. for expansions and it is negative for  $u_L < u_R$ , i.e. for contractions. In other words, for local contractions, the FOU-MC-E advection scheme gives a negative contribution to the backwater, i.e. the advection term causes an erroneous increase in energy head, as already recognized by [Stelling and Duinmeijer \(2003\)](#); [Kramer and Stelling \(2008\)](#) for the flow over sudden contractions (flow over a saw-tooth bottom and over a weir).

In agreement with [Stelling and Duinmeijer \(2003\)](#); [Kramer and Stelling \(2008\)](#), one can conclude that for (strong) local contractions with sudden flow variation, the hydrostatic pressure assumption is not valid and equation ((2.4)) should be applied with care. In such flow situations, switching locally between the FOU-EHC (at contractions) and the FOU-MC-E scheme (elsewhere), provides more physically correct results.

## 4 Momentum advection on unstructured/irregular grids

In this section we switch from rectangular grids to curvilinear and triangular grids. We have tested four multi-purpose 2D/3D modelling systems for their numerical backwater due to advection and grid effects and for their conservation properties. The results are presented in Section 6 for the different tests presented in section 5. In the sections below we briefly describe the applied systems and their advection schemes. For details, we refer the reader to the mentioned literature.

### 4.1 TELEMAC

The TELEMAC system uses a triangular finite element discretization and solves the two-dimensional, depth-averaged (TELEMAC-2D) or three-dimensional (TELEMAC-3D) Reynolds-averaged Navier-Stokes equations. For details, we refer the reader to e.g. Galland *et al.* (1991); Jankowski (1999); Weilbeer *et al.* (1999); Hervouet and Jankowski (2000); Hervouet (2007). In TELEMAC, the advection terms can be approximated using the method of characteristics, which is very similar to the Eulerian-Lagrangian approach used in UnTRIM. Other options are using the Streamline Upwind Petrov-Galerkin (SUPG) method or using a (Multi-dimensional Upwind) Residual Distributive (MURD) scheme Abgrall and Mezine (2003); Ricchiuto *et al.* (2007); Ricchiuto and Bollermann (2009). Depending on the choice for the advection method, also the time integration scheme is altered. Either a fractional step approach or a Crank-Nicolson method is used to proceed the solution in time.

In this work we test the following advection schemes:

Advection scheme 1 : The characteristic scheme: *Telemac char* (advection option 1)

Advection scheme 2 : The SUPG scheme: *Telemac SUPG* (advection option 2)

Advection scheme 3 : The MURD-N scheme: *Telemac MURD-N* (advection option 14)

The results obtained with Telemac were run with a Courant number  $C \approx 1$ . Larger and smaller time steps were tested, but mostly degraded the results, or increased sensitivity to either grid resolution or structure.

### 4.2 D-Flow Flexible Mesh

D-Flow Flexible Mesh (D-Flow FM) solves the 2D and 3D shallow water equations on structured or unstructured grids, using a finite volume approach. The system employs a semi-implicit time discretization similar to the UnTRIM model described in section 4.4. The advection terms are discretized explicitly, with a spatial discretization derived from Perot (2000). The idea is that the momentum advection vector is computed for computational cells (cell-centered) and then re-mapped to the cell faces. In this way, it is claimed that a momentum-conservative discretization is obtained for steady flow. For unsteady flow, momentum conservation can not be guaranteed due to the semi-implicit discretization. The advection terms are discretized in an upwind manner. For each cell the incoming and outgoing momentum is computed using upwind fluxes, where the upwind velocity vectors can be computed with first or second order accuracy, applying a slope limiter. Second order accuracy is obtained for smooth solutions, through an extended stencil, see section 2.8. The slope limiter makes sure the solution remains stable and (near) monotone for discontinuous solutions. For such situations, the approximation reduces to first order, by virtue of the limiter.

During the present investigations, we noted the following. The limiter in D-Flow FM is applied with a factor  $f_{lim} = (1 - CFL)$ , for stability and temporal accuracy. It is required due to

the (explicit) forward-Euler time discretization of the advection term. The  $f_{lim} = (1 - CFL)$  mimics the transfer of data along a characteristic line. However, this causes the discretization to reduce the spatial accuracy in and around steady states to just over order 1. With the factor  $f_{lim} = (1 - CFL)$ , the time step can be such that the Courant number is below  $C \approx 0.7$ . Without the factor, the time step needs to be reduced to Courant numbers  $C < 0.05 - 0.5$  for stability reasons (depending on the chosen limiter: 0.05 for the Van Leer limiter; 0.25 for the MinMod limiter). For higher Courant numbers, the computation does not become unstable, but instabilities are initiated occasionally, which are then damped, due to the fact that the limiter then reduces the scheme (locally) to first order. Stationary solutions, however, are not attained for this model setting.

In this work we test the following advection schemes:

Advection scheme 1 : The first-order accurate Perot-based scheme: *D-Flow FM Perot1*

Advection scheme 2 : The second-order accurate Perot-based scheme (using the MinMod limiter): *D-Flow FM Perot2*

The tests with the first-order scheme were run with a variable time step steered by the condition that the maximum local Courant number  $C < 0.7$ . For the second-order scheme a maximum local Courant number  $C < 0.3$  was applied, again with variable time step steering.

#### 4.3 Delft3D

The hydrodynamic core of Delft 3D [Deltas \(2013\)](#) discretizes the governing flow equations using finite differences on a staggered, curvilinear grid. Time integration is performed using an Alternating Direction Implicit (ADI) solution strategy [Leendertse \(1967\)](#), where a time step is split in two stages. The advection terms in the momentum equation can be handled with three different schemes: (i) the *Cyclic*-scheme [Stelling and Leendertse \(1992\)](#), (ii) the *WAQUA*-scheme (which closely resembles the advection scheme applied in the *WAQUA*-modelling system [Zijlema \(1999\)](#)), and (iii) the *Flooding*-scheme (which is the advection scheme applied in the Delft-FLS-system, see e.g. [Stelling and Duinmeijer \(2003\)](#)).

With the application of the *WAQUA*- or the *Cyclic*-method in the ADI scheme, the discretization of the advection terms alternates, between explicit and implicit and second-order upwind and central. The *WAQUA* scheme only applies the (explicit) second-order upwind discretization in only one of the two grid directions, whereas the *Cyclic* method applies it in both directions (alternatively with the implicit central discretization). The *WAQUA*-scheme and the *Cyclic* method impose a mild restriction on time step for stability (a guideline is  $C < 2$  for dynamic computations, but  $C$  should be smaller for steady-state computations ([Stelling \(1983\)](#))). The *Flooding*-scheme can be applied for problems that include rapidly varying flows for instance in hydraulic jumps and bores. When applying the *Flooding*-scheme, the integration of the advection term is explicit and the time step is restricted by the Courant number for advection.

For more elaborate descriptions of the conceptual and numerical approaches applied in Delft 3D-FLOW, see [Deltas \(2013\)](#).

In this work we test the following advection schemes:

Advection scheme 1 : The Cyclic scheme: *Delft3D Cyclic*

Advection scheme 2 : The Flooding scheme: *Delft3D SD(2003)*

Advection scheme 3 : The WAQUA scheme: *Delft3D WAQUA*

Tests were run with a fixed time step. In general, the Cyclic scheme allowed the largest Courant numbers ( $C \approx 1$ ), whereas the WAQUA schemes requires Courant numbers between 0.3 and 0.6 and the flooding scheme between 0.05 and 0.3.

#### 4.4 UnTRIM

The numerical modelling system UnTRIM has been developed as the unstructured grid variant [Casulli and Walters \(2000\)](#); [Casulli and Zanolli \(2002\)](#) of the structured grid system TRIM [Casulli \(1990\)](#); [Casulli and Cheng \(1992\)](#). It can be applied on structured, unstructured and hybrid grids. The advection terms are modelled using an Eulerian-Lagrangian approach, tracing back along local streamlines. This approach does not conserve momentum. In practice, the method is unconditionally stable.

For UnTRIM we can only test the available Eulerian-Lagrangian (or characteristic) advection scheme (similar to the scheme in section 2.9, but the exact implementation details of UnTRIM are not known to the author):

Advection scheme 1 : Eulerian-Lagrangian: *UnTRIM char*

The UnTRIM tests were run with Courant number between 0.4 and 3. The results shown were obtained with  $C \approx 1$ .



## 5 Numerical experiments

We now aim to verify the findings from section 3 using numerical experiments and quantify the contribution to the backwater or total head loss due to the advection discretization for the flow over variable topography. As a reference, we take an existing numerical model for a stretch of the Elbe river, between the German cities of Lauenburg and Geesthacht ([Platzek et al. \(2016\)](#)). From this model, we construct a series of tests with increasing complexity, that schematically represents the geometrical variation along the river stretch: the overall bed slope, bed forms and groynes (leaving bends outside the present investigation). We obtain three schematic 1D tests, two schematic 2D tests and the actual river case study:

- Test 1 : Uniform channel flow along a constant slope (1D)
- Test 2 : Flow over a wavy bed without bottom friction (1D)
- Test 3 : Flow over a sloped wavy bed with bottom friction (1D)
- Test 4 : Flow over a sloped wavy bed with bottom friction and emerged groynes (2D)
- Test 5 : Flow over a sloped wavy bed with bottom friction and submerged groynes (2D)
- Test 6 : Case study: Elbe river from Lauenburg to Geesthacht (2D)

The topography and water levels for the five schematic tests are illustrated in 1D in Fig. 5.1. For each of these tests, the channel has the same dimensions. It has a length  $L = 1000$  m and width  $W = 240$  m. At the upstream boundary a discharge  $Q = 960 \text{ m}^3/\text{s}$  is prescribed. At the downstream boundary the water level is fixed at  $\zeta = 8$  m, which is also the initial condition. The initial flow velocity is  $u = v = 0$  m/s. We define a reference bottom height  $h_{ref} = 4$  m on which all different geometry variations are super-positioned.

In all schematic tests, except for the uniform channel flow test, the channel bottom contains bed forms, which are described by a cosine function in the longitudinal  $x$ -direction. The bottom profile with the bed forms is described by the function:

$$h_b(x, y) = h_{ref} + A_b \cos(f_b x) \quad (5.1)$$

where  $h_b(x, y)$  is the bottom height (positive upwards) and  $A_b$  is the wave/bed form amplitude. The frequency  $f_b$  determines the length of the 'bed forms' and is defined as  $f_b = 2\pi n_b / L$ , where  $n_b$  is the number of bed forms within the domain (see Table 5.1).

For the groyne tests (tests 4 and 5), seven cosine-shaped groynes – extending over half of the channel width – are super-positioned on top of the sloped wavy bottom, i.e. the main channel and groyne fields have the bottom geometry containing the bed forms from test 3. The length of the groyne fields  $L_{gf}$  was chosen to be 110 m. At the position of the groynes, the topography is described by:

$$h_g(x, y) = h_{ref} + A_b \cos(f_b x) + A_g (1 + \cos(f_g(x - x_{gs}))) \quad (5.2)$$

where  $A_g$  is the groyne amplitude (half of the height) and  $x_{gs}$  is the  $x$ -coordinate where the cosine of each groyne starts (the middle of the previous groyne +  $L_{gf}$ ). The frequency  $f_g$  follows from the chosen 'width of the groyne'  $W_g$  and is defined as  $f_g = 2\pi / W_g$ . The geometrical parameters of all the tests are presented in Table 5.1.

For all five schematic tests and for the nine schematic advection schemes, we apply four recursively finer grids, to investigate the convergence properties and grid dependency of the schemes:

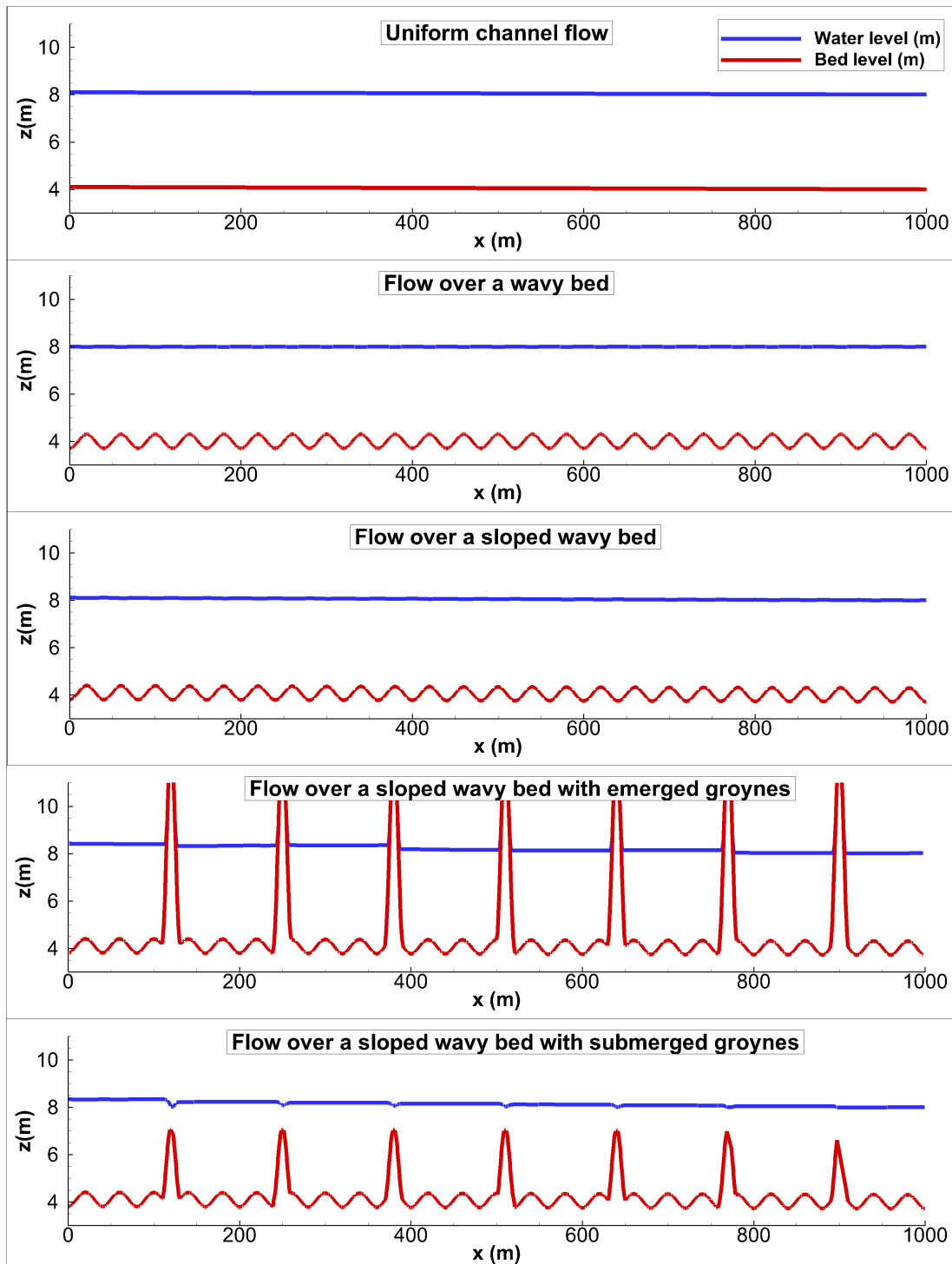


**Figure 5.1:** Schematic 1D depictions of water level and topography for tests 1–5 (longitudinal cross-section at  $y = 60$  m).

**Table 5.1:** Topography definitions for the five schematic tests. <sup>a</sup> The maximum Froude number  $Fr^{max} \approx 1$  at the most upstream groyne for the emerged groyne case.

<b>Test</b>	<i>L</i> (m)	<i>W</i> (m)	<i>h<sub>ref</sub></i> (m)	<i>i<sub>b</sub></i> (-)	<i>C<sub>z</sub></i> ( $\sqrt{m/s}$ )	<b>Parameter</b>							<i>Fr<sup>max</sup></i> (-)
						<i>n<sub>b</sub></i> (-)	<i>L<sub>b</sub></i> (m)	<i>A<sub>b</sub></i> (m)	<i>n<sub>g</sub></i> (-)	<i>W<sub>g</sub></i> (m)	<i>A<sub>g</sub></i> (m)	<i>L<sub>gf</sub></i> (m)	
1	1000	240	4	$10^{-4}$	50	0	0	0	0	0	0	0	0.16
2	1000	240	4	0	$\infty$	25	40	0.3	0	0	0	0	0.17
3	1000	240	4	$10^{-4}$	50	25	40	0.3	0	0	0	0	0.17
4	1000	240	4	$10^{-4}$	50	25	40	0.3	7	20	3	110	0.36
5	1000	240	4	$10^{-4}$	50	25	40	0.3	7	20	1.5	110	0.7 <sup>a</sup>

Resolution 1 :  $\Delta x = 10$  m (4 cells per bed form)

Resolution 2 :  $\Delta x = 5$  m (8 cells per bed form)

Resolution 3 :  $\Delta x = 2.5$  m (16 cells per bed form)

Resolution 4 :  $\Delta x = 1.25$  m (32 cells per bed form)

For the Elbe river test, also 4 recursively finer resolutions ranging from  $\Delta x = 16$  m to  $\Delta x = 2$  m are applied.

For the modelling systems with unstructured or curvilinear grids, we test four different grid structures, to investigate the effect of the grid structure on the backwater:

Grid structure 1 : Regular quadrilateral (cartesian) grid

Grid structure 2 : Irregular quadrilateral grid

Grid structure 3 : Regular triangular grid

Grid structure 4 : Irregular triangular grid

For each of the four grid structures we test three different resolutions:  $\Delta x \approx 10m$ ,  $\Delta x \approx 5m$  and  $\Delta x \approx 2.5m$ . It should be noted that for the irregular triangular and quadrilateral grids (grid types 2 and 4), the bed forms and groynes are not guaranteed to be positioned on grid lines and part of the bed level heights can be lost in the interpolation to the cell centres, faces and/or corners.

For all tests performed with the structured-grid code (section 2), the time step is determined dynamically based on a prescribed Courant number  $C = |u^{\max}| \Delta t / \Delta x$  and the maximum flow velocity  $u^{\max}$ . For the first-order schemes, the Courant number was fixed at  $C = 0.7$  and for the second-order schemes at  $C = 0.2$ , for maintaining stable solutions. The maximum Froude number  $Fr^{max} = u / \sqrt{gH}$  was also determined for all cases and added to Table 5.1.

## 5.1 Uniform channel flow

For this test, the channel described above has a bottom slope  $i_b = 1 \times 10^{-4}$  m/m (see Table 5.1), sloping from  $z = 4.1$  m to  $z = 4$  m ( $h_{ref}$ ), giving the channel an equilibrium depth of  $H^{eq} = 4$  m. Combined with a Chézy bottom roughness  $C_z = 50$   $m^{1/2}/s$ , this results in a flow velocity  $u = C_z \sqrt{H i_b} = 1$  m/s, which matches the boundary condition described above. For this test, the advection term should be zero.

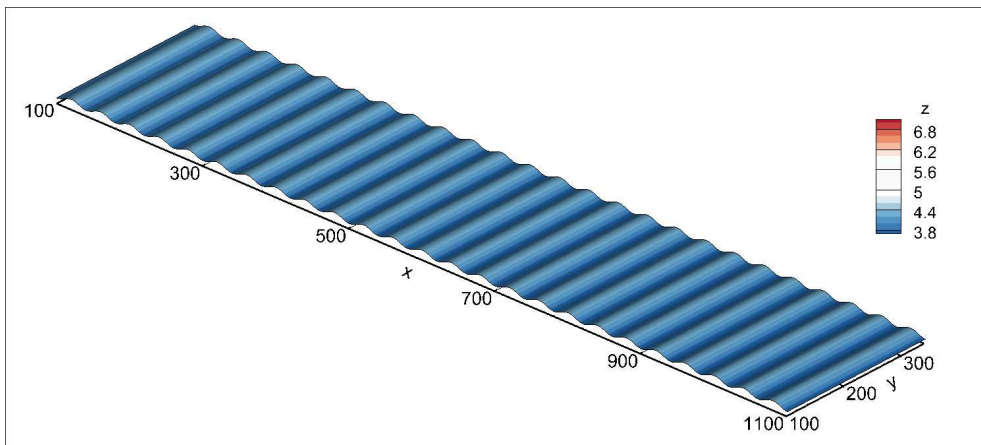


**Figure 5.2:** Bottom topography for the wavy bed test.

## 5.2 Flow over a wavy bed

As described above, the channel bottom is described by a series of 25 cosines (wave length  $L_b = 40$  m) forming a wavy bed in the longitudinal  $x$ -direction (see Table 5.1). The amplitude of the bed forms is  $A_b = 0.3$  m, causing the total water depth to vary approximately from  $H = 3.7$  to  $4.3$  m. In the lateral  $y$ -direction, the bottom is constant. There is no general slope in the bed and the bottom friction is switched off:  $\gamma = 0$ . The bottom topography is shown in Fig. 5.1.

For the steady and inviscid flow over a smooth bottom at low Froude numbers the analytical solution can be computed based on the principles of mass and momentum conservation. For this simple flow situation, the momentum equation reduces to the Bernoulli equation upon integration (formally along a streamline):

$$u \frac{\partial u}{\partial x} + g \frac{\partial \zeta}{\partial x} = 0 \Rightarrow \quad (5.3)$$

$$\frac{1}{2} u^2 + g \zeta = E \quad (5.4)$$

where  $E$  is an integration constant, being the total (kinetic + potential) energy (divided by the density) in the system. It can be determined using the continuity equation and the boundary condition:  $E = g \zeta_{BC} - \frac{1}{2}(q/H_{BC})^2$ , where  $\zeta_{BC}$  is the water level prescribed e.g. at the downstream boundary and  $H_{BC}$  is its corresponding total water depth. This system of equations can be reduced to a single equation by substituting the steady 1D continuity equation  $u = Q/(WH) = q/H$  in to the Bernoulli equation. After some algebra one ends up with the following cubic relation for the unknown total water depth  $H = H(x)$ , depending also on the bottom topography  $h = h(x)$  (see e.g. also [Ricchiuto \(2015\)](#)):

$$H^3 + \left( h - \frac{E}{2g} \right) H^2 + \frac{q^2}{2g} = 0 \quad (5.5)$$

This equation can be solved e.g. using Cardano's formula, or iteratively using Newton iterations. The solution for  $u$  is then obtained from  $u = q/H$ . The expressions for  $H$  and  $u$  are lengthy and therefore omitted, but as can be expected, they show an alternating wavy pattern. For this test, it is important that there should be no energy losses (zero bottom friction) and therefore no global backwater. The water level at the entrance of the channel should also be at  $\zeta = 8$  m. Any backwater in the experiment must come from numerical dissipation.

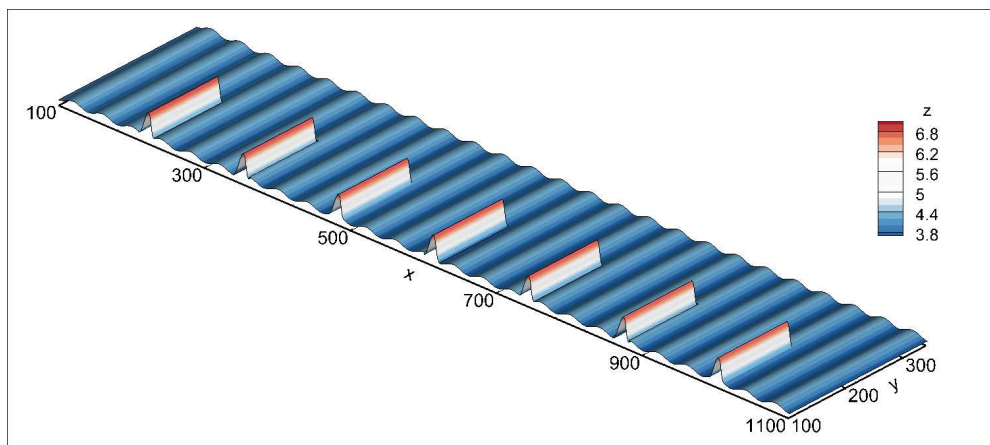


**Figure 5.3:** Bottom topography for the flow over a sloped wavy bed with groynes.

### 5.3 Flow over a sloped wavy bed with bottom friction

In this test the uniform channel flow (with bottom friction) and the inviscid wavy bed test are combined. The bottom topography for the sloped wavy bed test is the same as for the wavy bed case, except for an additional downward slope of  $i_b = 1 \times 10^{-4}$  m/m. Additionally, the bed friction is set to  $C_z = 50$  m<sup>1/2</sup>/s again. The test settings are summarized in Table 5.1. The reference solution for this test was obtained by a step method (or Keller-Box scheme) integrating the momentum equation (now including bottom friction) from the downstream boundary upwards.

### 5.4 Flow over a sloped wavy bed with emerged groynes

In this test, we add groynes to the sloped channel with wavy bed forms. Seven schematic groynes (described by cosine waves), with a groyne width in stream-wise direction  $W_g = 20$  m are added. The groynes extend over half of the channel width, i.e. the groynes are 120 m long. The groyne fields between the groynes have a length  $L_{gf} = 110$  m. In this first test, the groynes have a height of 6 m (twice the cosine amplitude of the groyne  $A_g = 3$  m) and are therefore emerged, see Table 5.1. The bottom topography for the flow over a sloped wavy bed with groynes is shown in a longitudinal slice in Fig. 5.1 and in a 3D view in Figure 5.3.

### 5.5 Flow over a sloped wavy bed with submerged groynes

For this test, only the cosine amplitude (half of the height) of the groynes is modified. The groynes obtain a reduced height of 3 m ( $A_g = 1.5$  m) and are, therefore, approximately 1 m submerged. All other parameters for this test are identical to the emerged groynes test of the previous section, see Table 5.1. A longitudinal slice of the topography and water level is displayed in Fig. 5.1.

By comparing the results of the emerged and the submerged groynes case, one can investigate the effect of *lowering the groynes*, an important topic of discussion for river maintenance and flood protection issues (see e.g. [Busnelli et al. \(2011\)](#)).

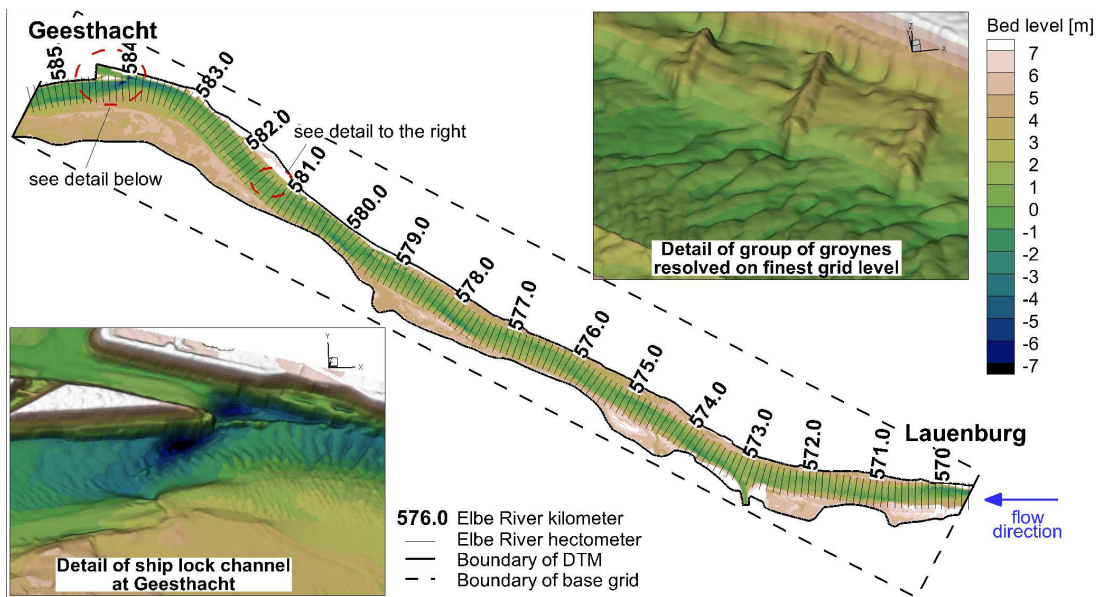


**Figure 5.4:** The Elbe River model: Digital Terrain Model (DTM) ( $2 \times 2$  m) for the Elbe River between the city of Lauenburg and the weir at Geesthacht. The 3D detail figures of the topography are ten times vertically exaggerated, compared to the horizontal scale. Copyright ©2016 John Wiley & Sons, reprinted with permission from Platzek et al. (2016).

## 5.6 The Elbe River from Lauenburg to Geesthacht

The final test is the case study from which we derived the schematic tests. It concerns a reach of the Elbe River between the cities of Lauenburg and Geesthacht in Germany, which is approximately 17 km long and – including the floodplains – 2.5 km wide (see Fig. 5.4). The stretch contains natural bed forms with similar characteristics as the wavy bed cases and it contains groynes which are emerged near the bank and submerged near the groyne tip, for the chosen discharge. All parameters for this test were taken from Platzek et al. (2016).

## 6 Results

We have performed the 6 different tests, applying the 9 different advection schemes on rectangular grids, and the 9 different schemes from the modelling systems from section 4, on unstructured/irregular grids. For each combination we tested at least 3 different resolutions. In total approximately 600 tests were executed. In this section we present the relevant results from all the different tests. For each test we first present the results on rectangular grids with the advection schemes from section 2 and then the results on different grid structures using the modelling systems from section 4. For the tests on the rectangular grids, we inspect the dependence of the numerical backwater on the properties of the momentum advection scheme and aim to formally establish the grid convergence rates. For the irregular/unstructured grid tests, we investigate the numerical/artificial backwater due to the combination of the grid structure and the advection scheme and also establish the behaviour of the error with (global) grid refinement.

The tests on rectangular discretizations were performed using the 2D depth-averaged model from [Platzek et al. \(2016\)](#). Using this model it is possible to compute the different contributions (bottom friction and advection) to the total backwater over the domain (mostly suited for 1D applications) and establish the behaviour of these contributions with grid refinement. The different contributions to the backwater are computed numerically in the same way as for the analysis in section 3, i.e. by integrating the corresponding terms (pressure, advection, bottom friction) over the length of the channel and scaling with  $g$ . For the 2D tests, an additional averaging over the width of the channel is performed. We express the backwater or head loss  $\Delta H$  at the inflow boundary in % of the backwater due to bottom friction over the same channel length. For test 2, where we only have the bed forms and no bottom friction, the backwater from test 3 is used as a reference. For the two groyne tests and for the Elbe river case no analytic solution is available and the runs with the smallest backwater are taken as reference.

We have seen from the analysis in section 3, that the numerical backwater contribution from the momentum advection discretization can be positive or negative. For this purpose, we have chosen the backwater (or upstream water level difference) as the error norm and not a strictly-positive mathematical error norm (e.g.  $L_\infty$ ,  $L_1$  or  $L_2$ ), as it would not show the difference between a positive or negative backwater effect. To illustrate the order of convergence for tests 2 and 3 (where an analytical solution is available), we include the convergence rates for the different schemes, based on the  $L^1$  norm of the water level:

$$p^l = \frac{\log\left(\frac{L_1^{l-1}}{L_1^l}\right)}{\log(2)}, \quad \text{for } l = 2, 3, \dots, l^{\max} \quad (6.1)$$

with

$$L_1^l = \frac{1}{I^l} \sum_{i=1}^{I^l} \left| \zeta_i^l - \zeta_i^{analytic} \right| \quad (6.2)$$

where  $l$  is the grid level within the convergence study and  $I^l$  is the number of grid cells in  $x$ -direction on grid  $l$ . The convergence rate then gives the order of the scheme:  $O(\Delta x^p)$ .

For the 2D tests we also inspect the velocity patterns, to see whether qualitatively correct results are obtained.

It is to be noted that not all combinations of modelling systems and grid structures were possible: Delft3D can only handle rectangular and curvilinear grids and Telemac can only

compute on triangular grids. For the other combinations, therefore, no results are available. These combinations are left open in the figures in the following sections.

## 6.1 Uniform channel flow

For the uniform channel flow test, the correct solution consists of a uniform velocity and equilibrium depth, which can be computed based on the bottom roughness in the form of the Chézy coefficient  $C_z$ , the channel slope  $i_b$ , the channel width  $B$ , the depth  $H$  and the discharge  $Q$ :

$$u^{eq} = C_z \sqrt{H^{eq} i_b} \quad (6.3)$$

and

$$H^{eq} = \frac{Q}{u^{eq} * B} \quad (6.4)$$

For the chosen setup, this results in a water level that is sloped downward along the channel from  $\zeta = 8.1$  m to  $\zeta = 8$  m, resulting in a constant total water depth  $H^{eq} = 4$  m. Any deviation must come from errors made in the advection discretization or from the boundaries.

### 6.1.1 Results on rectangular grids

In this test, bottom friction causes the water level to be sloped downward along the channel from  $\zeta = 8.1$  m to  $\zeta = 8$  m, resulting in a constant total water depth  $H = 4$  m. Any deviation must come from errors made in the advection discretization or from the boundaries. The largest deviation of the water level at the upstream boundary, i.e. the numerical head loss or backwater, over all four resolutions, drops from  $-5 \times 10^{-4}$  m on the coarsest resolution of  $\Delta x = 10$  m to  $-5 \times 10^{-5}$  m. For the backwater  $\Delta H = 10$  cm over the length of the channel, this is a spurious contribution of -0.5 to -0.05 % due to discretization errors. No significant differences were found between the different advection schemes. For this test, it can therefore be concluded that – as expected – advection plays no significant role, and only bottom friction causes the backwater. The implementation of the boundary conditions played a larger role in the total backwater than the advection schemes.

### 6.1.2 Results on irregular/unstructured grids

The results obtained using the different modelling systems on the different grid structures, on the 3 grid resolutions showed deviations from the analytical solutions that varied between -0.9 and +0.08 %. It can thus be concluded that for uniform flow (no flow variation), any grid irregularities do not introduce large disturbances for the tested modelling systems.

## 6.2 Flow over a wavy bed

For this test, the bottom friction is zero, but the bed level varies, causing gradual flow variation (due to the Bernoulli effect), which should occur without energy losses. In other words, the backwater for this test should be zero. To be able to compare the numerical/artificial backwater effect due to discretization errors with a certain reference backwater (we cannot divide by zero), the reference backwater for this test was taken from the test with sloping wavy bottom and with bottom friction (i.e. from section 6.3). The backwater for that test results from bottom friction. For the sloped channel without the wavy bottom, the backwater effect equals the difference in bed level between the upstream and downstream end of the channel, i.e.  $L \times i_b = 1000 \times 10^{-4} = 10$  cm. Due to the additional resistance of the flow accelerations over the wavy bed, the backwater for the sloped wavy bed adds up to 10.2 cm (instead of the 10 cm for the sloped uniform channel flow).

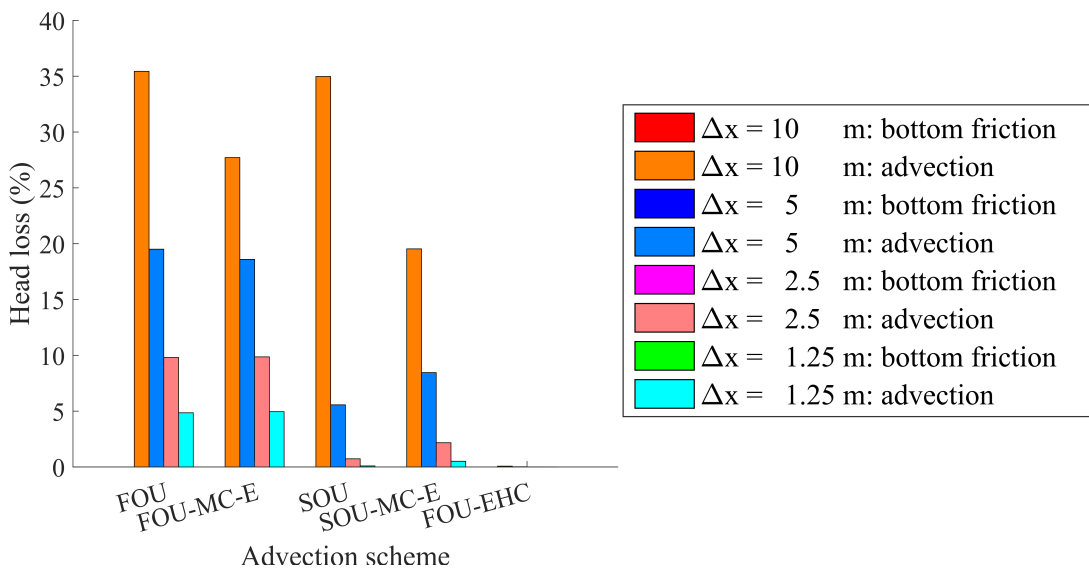


**Figure 6.1:** Total head loss for the flow over a wavy bed, for the five advection schemes from the analysis and all four grid resolutions. For this (inviscid) case, the bottom friction contribution is zero.

### 6.2.1 Results on rectangular grids

Figure 6.1 shows the upstream head loss (or backwater) for the five advection schemes from the analysis, and the four grid resolutions. It can be seen that depending on the advection scheme, the numerical head loss can be as high as 36 % of the backwater due to bottom friction, amounting to an artificial (additional) backwater of 3.6 cm. As was demonstrated using the analysis in section 3, the FOU-EHC scheme shows (almost) no backwater. The small backwater on the coarsest grid ( $\approx 8\%$ ) comes exclusively from the downstream boundary, due to a discrepancy in discretely representing the exact bed level at the boundary. Over the channel there is no additional build-up of the backwater. Additional tests with an improved boundary treatment, demonstrate that the artificial backwater for the FOU-EHC scheme can be reduced to below 0.1 %, even on the coarsest grid.

As expected, the second-order schemes perform better than their first-order counterparts. This can be also verified based on the  $L_\infty$  norms and convergence rates that have been determined for the five schemes from the advection scheme analysis from section 3, see Table 6.1. The second-order schemes indeed show second-order convergence rates. However, in particular on the coarser grids, their performance is similar to or even worse than their first-order counterparts. The FOU-EHC scheme then provides much less backwater, despite being only first-order accurate. This is a result of the constancy/conservation properties of the scheme, concerning the energy height.

The relatively good performance (low artificial backwater) for the Eulerian-Lagrangian scheme, might be due to the substepping approach and the second-order accurate interpolation during the tracking and at the foot of the trajectory. This, however, has not been verified.

**Table 6.1:**  $L_\infty$  norms and convergence rates  $p$  for the different advection schemes, for tests 2 and 3 (flow over a wavy bed and over a sloped wavy bed).

<b>Advection scheme</b>	<b>Grid resolution</b> $\Delta x$ (m)	<b>Test 2: wavy bed</b>		<b>Test 3: sloped wavy bed</b>	
		$L_\infty$ norm (m)	Convergence rate $p$	$L_\infty$ norm (m)	Convergence rate $p$
FOU	10	$4.2 \times 10^{-2}$	-	$4.0 \times 10^{-2}$	-
	5	$2.3 \times 10^{-2}$	0.98	$2.2 \times 10^{-2}$	0.97
	2.5	$1.2 \times 10^{-2}$	1.06	$1.1 \times 10^{-2}$	1.05
	1.25	$5.7 \times 10^{-3}$	1.05	$5.6 \times 10^{-3}$	1.04
FOU-MC-E	10	$3.4 \times 10^{-2}$	-	$3.3 \times 10^{-2}$	-
	5	$2.2 \times 10^{-2}$	0.75	$2.1 \times 10^{-2}$	0.75
	2.5	$1.1 \times 10^{-2}$	0.99	$1.1 \times 10^{-2}$	0.98
	1.25	$5.8 \times 10^{-3}$	1.03	$5.7 \times 10^{-3}$	1.02
FOU-EHC	10	$6.1 \times 10^{-3}$	-	$6.4 \times 10^{-3}$	-
	5	$3.1 \times 10^{-3}$	0.93	$3.3 \times 10^{-3}$	0.93
	2.5	$1.6 \times 10^{-3}$	0.98	$1.6 \times 10^{-3}$	0.98
	1.25	$7.9 \times 10^{-4}$	0.99	$8.4 \times 10^{-4}$	0.99
SOU	10	$3.7 \times 10^{-2}$	-	$3.6 \times 10^{-2}$	-
	5	$6.1 \times 10^{-3}$	2.92	$6.1 \times 10^{-3}$	2.87
	2.5	$8.9 \times 10^{-4}$	2.79	$9.5 \times 10^{-4}$	2.72
	1.25	$2.3 \times 10^{-4}$	2.12	$1.9 \times 10^{-4}$	2.17
SOU-MC-E	10	$2.6 \times 10^{-2}$	-	$2.5 \times 10^{-2}$	-
	5	$1.0 \times 10^{-2}$	1.45	$1.0 \times 10^{-2}$	1.43
	2.5	$2.6 \times 10^{-3}$	2.02	$2.6 \times 10^{-3}$	1.96
	1.25	$6.3 \times 10^{-4}$	2.10	$6.6 \times 10^{-4}$	1.95

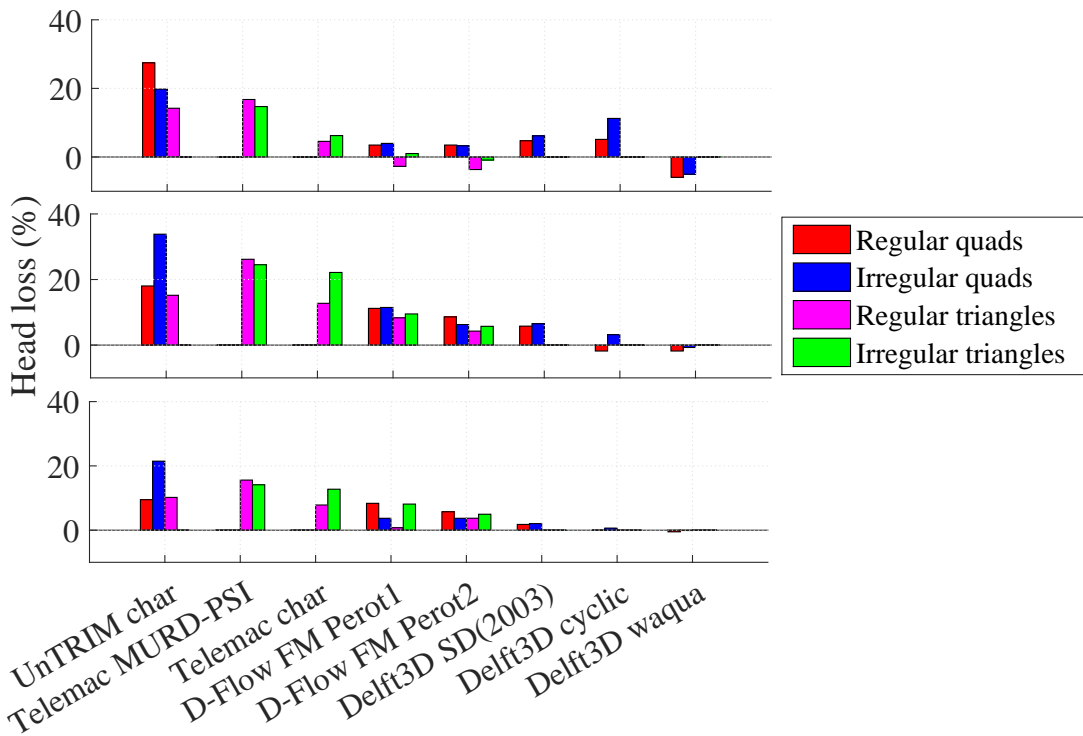


**Figure 6.2:** Numerical backwater for the flow over a wavy bed test, for the different advection schemes and grid structures of the four modelling systems, for the  $\Delta x \approx 10\text{ m}$  (top),  $\Delta x \approx 5\text{ m}$  (middle) and  $\Delta x \approx 2.5\text{ m}$  (bottom) resolution grid.

### 6.2.2 Results on irregular/unstructured grids

The numerical backwater for this test (in % of the backwater purely due to bottom friction), using the different modelling systems on the different grid structures and resolutions, is shown in Figure 6.2 (the bottom friction contribution has not been determined). It can be seen that the second- and third-order accurate schemes from Delft3D show the least artificial backwater. The maximum artificial backwater of 33.8 % as obtained using UnTRIM on an irregular quadrilateral grid with an average resolution of  $\Delta x = 5\text{ m}$  is comparable to the result obtained with the first order upwind scheme on the rectangular grid. From the figure it can also be noted that grid irregularity increases the backwater, as could be expected.

It should be noted that the UnTRIM results (obtained using the characteristic or semi-lagrangian advection scheme Casulli and Cattani (1994)) show a time step/Courant number dependency in the steady state. For larger Courant numbers the artificial backwater reduces and eventually becomes negative (i.e. increasing energy head in downstream direction). This can be seen in Figure 6.3.

### 6.3 Flow over a sloped wavy bed

Now we investigate to which extent the results from the previous test are also valid when combined with bottom friction (and a channel slope). For this test, the bed level variations interact with the quadratic bottom friction, resulting in a theoretical backwater and reference head loss of  $\Delta H^{ref} = 10.2\text{ cm}$  (obtained using numerical integration of the equations on a  $\Delta x = 0.5\text{ m}$  grid). We thus compute the total percentual upstream head loss  $100 \times (\zeta_{upstream} - \zeta_{upstream}^{ref}) / \Delta H^{ref}$  consisting of contributions both from the bed friction and from the advection term, for the different advection schemes and the four resolutions.

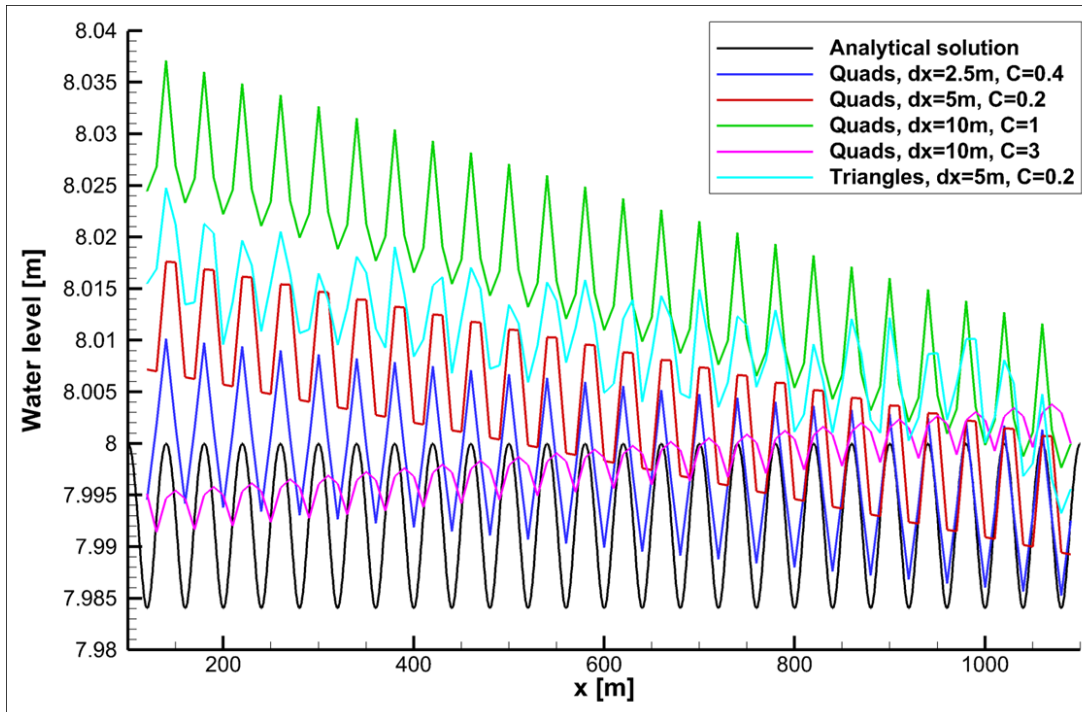


**Figure 6.3:** Numerical backwater for the flow over a wavy bed test using UnTRIM for different grid structures, resolutions and Courant numbers.

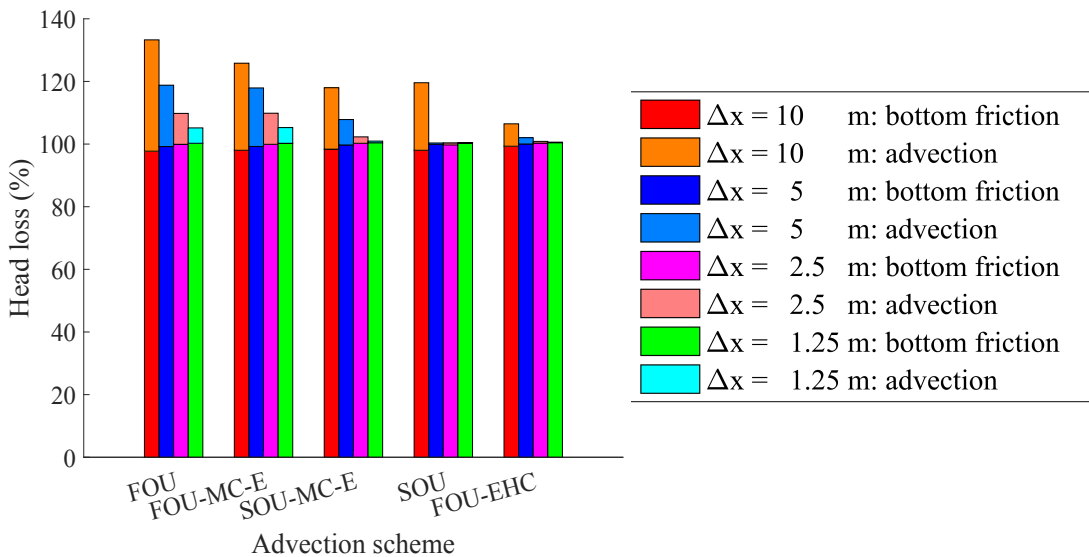
### 6.3.1 Results on rectangular grids

Figure 6.4 shows the upstream head loss contributions due to bottom friction and advection, for the five advection schemes from the analysis and the four grid resolutions. The maximum head loss of 132 % corresponds to 13.7 cm total head loss, instead of the 10.2 cm (100 %) for the analytic solution. The results are again sorted (left to right) from the scheme with the largest average total head loss over the four grids, to the scheme with the smallest average head loss.

From these results one can conclude that the common consensus that rivers are dominated by a *global* balance between pressure gradient and bottom friction (in the momentum equation) is not completely valid, due to the artificial backwater contribution from the advection approximation. For moderately coarse grids and for many advection schemes, the contribution of the advection term to the balance is of the same order as the backwater due to bottom friction.

The  $L_\infty$  norms and the convergence rates for the five schemes from the analysis in section 3 have been included in Table 6.1 also for this test. It can be seen that the inclusion of bottom friction has little effect on the convergence rates for the different advection schemes. As can be seen, also for this test, second-order accuracy is attained by the second-order schemes.

Additionally, Table 6.2 shows the average convergence rates of all nine different rectangular-grid schemes for this test. Again, the table also shows the numerical head loss for the 5 m resolution grid. Depending on the advection scheme, the numerical head loss can be 20 % of the head loss due to bottom friction. Here it can, among others, be seen that the Eulerian-Lagrangian scheme does show first-order convergence (as expected), but that the percentual backwater is low. This result might, however, be dependent on the chosen time step or Courant number.



**Figure 6.4:** Head loss for the flow over a sloped wavy bed on rectangular grids, for the five advection schemes from the analysis and the four grid resolutions. Displayed is the total head loss as a sum of the head loss due to bottom friction and the head loss due to advection.

**Table 6.2:** Flow over a sloped wavy bed: numerical head loss (%) due to advection errors for the 5 m grid and average convergence rates over the three finest grids for the different advection schemes.

Advection scheme	Numerical head loss $\Delta H_{num}$ (%)	Convergence
		rate $p$
FOU	19.9	1.00
FOU-SD	18.8	0.86
FOU-MC-E	18.7	0.86
FOU-MC-C	16.9	0.70
SOU-MC-E	8.7	1.78
EL	8.1	1.14
SOU-MC-C	8.0	1.53
FOU-EHC	3.1	1.18
SOU	2.8	2.59

### 6.3.2 Results on irregular/unstructured grids

The backwater for this test (in % of the backwater purely due to bottom friction), using the different modelling systems on the different grid structures and resolutions, is shown in Figure 6.5. Again only the (nett) numerical/artificial backwater (originating from advection errors) is displayed. The contribution to the backwater due to bottom friction has not been determined. The UnTRIM results for this test are not yet available.

Delft3D allows the user to investigate how large the contributions from the different terms in the momentum equation are (also locally). To investigate which terms dominate the local balance in the equation (for steady flow), we examined the distribution of these terms (pressure gradient, bottom friction, advection) along the channel centerline for a situation with reduced 0.05 m amplitude of the bed forms, see Figure 6.6. One can clearly see that even for such small bed forms, the *local* balance in the momentum equation is dominated by the pressure gradient and the momentum advection term. As is commonly acknowledged, the *global* balance in the equations is mainly between pressure gradient and bottom shear stress, but depending on the advection scheme it is found that an additional artificial backwater effect is

introduced by the momentum advection discretization. The size of this contribution depends on the chosen advection scheme.

## 6.4 Flow over a sloped wavy bed with emerged groynes

In this test, groynes are added to the test from section 6.3. The groynes have a height of 6 m above the bed and are therefore emerged. We now inspect the effect of such groynes on the backwater and more specifically, the dependency on the advection scheme. The total head loss again has two contributions: bottom friction and advection.

For the higher grid resolutions, no stationary solution was obtained. To investigate the numerical backwater for this situation, we determined temporal averages of the water level at the upstream boundary. In particular for the highest resolution, we found variations in time in the order of +/- 0.1 m. Given this large variation in the results, the values presented for this test, should mostly be viewed from a qualitative perspective.

### 6.4.1 Results on rectangular grids

Figure 6.7 shows the percentual head loss  $(\zeta_{upstream} - \zeta_{upstream}^{ref})/\Delta H^{ref}$  for the five schemes from the analysis. As no analytical solution is available for this test, we have taken the advection scheme with the least total head loss at the upstream boundary as the reference:  $\Delta H^{ref} = 35$  cm, as computed by the FOU-EHC scheme on the  $\Delta x = 1.25$  m grid (corresponding to a percentual head loss  $\Delta H = 100\%$ ). A 20 % head loss in the figure thus corresponds to 7 cm of additional head loss on top of the 35 cm.

From the figure three things can be noted. First, one can see that with an increased head loss due to advection, the head loss due to bottom friction decreases. Second, the convergence behaviour of the schemes is different. In particular the FOU-EHC scheme shows very little variation over the grids. Finally, it appears that the different schemes converge to different solutions. In particular the fine-grid results of the FOU and SOU scheme differ from the results of the other three schemes.

For the momentum-conservative scheme, the switch from a first- to a second-order advection scheme shows moderate influence on the backwater. The effect on the flow velocity and on the emergence of turbulent eddies is much greater. In Fig. 6.8, the  $z$ -component of the vorticity  $\vec{\omega} = \vec{\nabla} \times \vec{u}$  is displayed as projected on the free surface, for the FOU-MC-E and SOU-MC-E schemes for the three finest grids. It can be seen that with the first-order scheme, vortex shedding is much less pronounced than with the second-order scheme, in particular on the coarser grids.

### 6.4.2 Results on irregular/unstructured grids

The numerical backwater (in %) for this test, obtained on the different grid structures and resolutions, using the Telemac and D-Flow FM systems, is shown in Figure 6.9. The UnTRIM and Delft3D results are not yet available. From the figure, one can conclude that there is a considerable variation in the numerical/artificial backwater for the different schemes and modelling systems. The reference backwater has been chosen the same as for the computations on the rectangular grids.

D-Flow FM consistently produces a backwater larger than the reference over all grid resolutions, with an expected decrease in the artificial backwater with increasingly finer grids. Controversely, Telemac produces a total backwater which is less than the reference on the coarser grids, which then increases to similar values as for D-Flow FM on the finer grids.

Additionally, it can be seen that the backwater is less on all structured grids than on the unstructured/irregular grids, as was to be expected. The effect can, however, be a factor two, which is considerable.

## 6.5 Flow over a sloped wavy bed with submerged groynes

In this test, the groynes from the previous test are lowered such that they become submerged (with the groyne crest approximately 1 m below the free surface). For this case the reference upstream water level (obtained in a similar way as for the emerged groynes case) is  $\zeta_{up} = 8.16$  m. By comparing the results with the test with emerged groynes, one can investigate the effect of lowering the groynes in a river section (see e.g. [Busnelli et al. \(2011\)](#)). Below we demonstrate, that depending on the chosen advection scheme and the grid resolution, the effect of lowering the groynes can be in the order of 9–23 cm.

### 6.5.1 Results on rectangular grids

Figure 6.10 shows the percentual head loss for the five different advection schemes from the analysis and the four grid resolutions. The reference solution for this test was taken to be the solution obtained with the FOU-EHC scheme on the finest grid resolution with  $\Delta x = 1.25$  m, with a total head loss of 16.4 cm, corresponding to a 100 % head loss in the figure. This means that the 277 % head loss in the figure – as obtained using the FOU scheme on the coarsest grid with  $\Delta x = 10$  m, gives a total head loss of 45.4 cm, i.e. an additional backwater of 29 cm over 1000 m of channel length, due to the advection discretization.

Again, we can deduce several things from the figure. First, the head losses for this test are much larger than for the previous tests. Second, it can be seen that on the finer grids the FOU, FOU-MC-E and SOU-MC-E schemes provide similar head losses  $\Delta H \approx 140 – 150$  %. We know that – in reality – vertical recirculation zones emerge behind the groynes, dissipating energy. This mechanism is, of course, not incorporated in our 2D, depth-averaged model. In civil engineering methods, these losses are commonly parameterized using Carnot losses for sudden expansions (see e.g. [Chanson \(2004\)](#)). From the analysis in section 3, we know that the FOU scheme gives exactly the Carnot loss for any (discrete) velocity variation. It appears that both momentum conservative schemes also tend towards this result. Additionally, it can be noted that these two schemes also show relatively little dependence on the grid resolution.

Finally, it can be seen that the FOU-EHC scheme provides a reduction in the backwater for the coarser grids. From the analysis, we know that the scheme does not give any head losses related to the velocity gradients. Therefore, the backwater is much less than for the other schemes. The increase in head losses with increased grid resolution, most likely comes from the better representation of the local accelerations over the groynes and therefore the increased bottom friction contribution. The advection contribution only varies between 4 and 8% over the grids. The FOU-MC-E scheme gives a significantly larger backwater than the FOU-EHC scheme and depending on the resolution a larger or smaller backwater than the FOU scheme (conform the results from section 3). It can also be seen that it shows relatively little variation over the range of grid resolutions.

By comparing the results with the test with emerged groynes, one can investigate the effect of lowering the groynes in a river section (see e.g. [Busnelli et al. \(2011\)](#)). Computing the difference in water levels for the two flow situations, for the different advection schemes and grid resolutions, the effect of lowering the groynes can be found to be in the range of 9–23 cm. Considering the fact that often river engineering projects involve man-induced modifications which result in water level changes of several centimeters to decimeters and that the river engineers commonly need to provide water level predictions with an accuracy below 5 cm, this result can be considered worrying.

### 6.5.2 Results on irregular/unstructured grids

The numerical backwater (in %) for this test, obtained on the different grid structures and resolutions, using the different modelling systems, is shown in Figure 6.11. It can be seen that for Telemac on the 5 m grid, the total backwater reduces quite significantly for irregular triangular grids. This is very likely caused by the fact that velocity gradients are not represented as accurately on irregular grids, reducing the advection term and thus also its spurious contribution to the backwater. This behaviour, however, was only established for the present test. It is to be noted, that the UnTRIM results for this test are not yet available. Using the Delft3D-WAQUA scheme the computations on the two finest grids showed wiggles. Only by adding a considerable amount of horizontal diffusion, the wiggles could be removed. The results are, therefore, not included.

Also for the flow over submerged groynes, we investigated the local balances of the different terms in the momentum equation in x-direction using Delft3D. The distribution of the different acceleration terms in the momentum equation in x-direction for the sloped channel with groynes are shown in Figure 6.12 for the longitudinal cross-sections at  $y = 75$  m (over the groyne),  $y = 125$  m (center of channel, near groyne tips) and  $y = 175$  m (main channel).

## 6.6 The Elbe River from Lauenburg to Geesthacht

Finally, we consider the actual case study from which we deduced the schematic tests and their topographical characteristics. Again, we apply all different schemes and modelling systems on the different grid structures and resolutions, and inspect the differences in the total backwater at the upstream boundary.

### 6.6.1 Results on rectangular grids

Figure 6.13 again shows the head loss for the five schemes from the analysis in section 3 and for the four grid resolutions. One can see that the variation in total head loss over the schemes is less than for the schematic test cases. For this case, the contribution to the total head loss from the bottom friction is more dominant than that from advection. Nonetheless, the maximum difference of 10.4 % corresponds to a water level difference of 22 cm over 17 km, from which one can again conclude that the uncertainty due to the advection scheme is quite significant. This needs to be counteracted by a reduced bottom friction, which may modify the flow patterns, specifically in shallow areas, reducing the reliability and applicability of the model, in particular for computations with different discharge-stages or for possible morphodynamic computations, relying on accurate bottom shear stress predictions.

However, the variation over the grids for the two momentum-conservative schemes and for the FOU-EHC scheme is relatively small, rendering them more reliable than the FOU and SOU schemes. It can thus be concluded that the conservation/constancy properties related to momentum and/or energy head are more important than the order of the scheme, when the aim is obtaining accurate, reliable and grid-insensitive water level predictions.

### 6.6.2 Results on irregular/unstructured grids

The river case was only tested using Telemac (section 4.1) and D-Flow FM (section 4.2). For both of these systems several of the available advection schemes were tested. For Telemac, we tested four different advection schemes: 1) the characteristic scheme, 2) the SUPG scheme, 3) the MURD-PSI scheme and 4) the edge-by-edge implementation of the MURD-N scheme. These schemes were tested because they are either recommended and/or currently applied in project work. For D-Flow FM we tested the Perot based scheme with first-order upwind velocities in the advective fluxes and with second-order accurate upwind velocity interpolation (with Monotonized-Central limiter).

For Telemac we tested on regular triangles (halved quadrilaterals) and on irregular triangles. D-Flow FM was tested on a hybrid grid (quadrilaterals and triangles combined) and on the same irregular triangle grid as used for Telemac.

We first inspected the water levels along the fairway (river axis shifted towards the deepest parts of the channel). For Telemac, the results obtained on regular triangles are shown in Figure 6.14. A comparison between Telemac and D-Flow FM is provided in Figure 6.15. Figure 6.16 shows the water levels in the whole domain as obtained using D-Flow FM on irregular triangles. The figure also shows the partitioning (or domain decomposition) used for the MPI-parallelization.

Inspecting the velocity distributions in a region near the Elbe Seitenkanal, we obtain the flow patterns for advection scheme 1 ("characteristics") and 14 ("MURD N-scheme") as depicted in Figure 6.17.

It can be seen that the characteristic scheme does not reproduce the correct extent and strength of the circulation pattern (vortex) that is to develop in the mouth of the Elber Side channel. Measurements have confirmed the emergence of such a circulation.

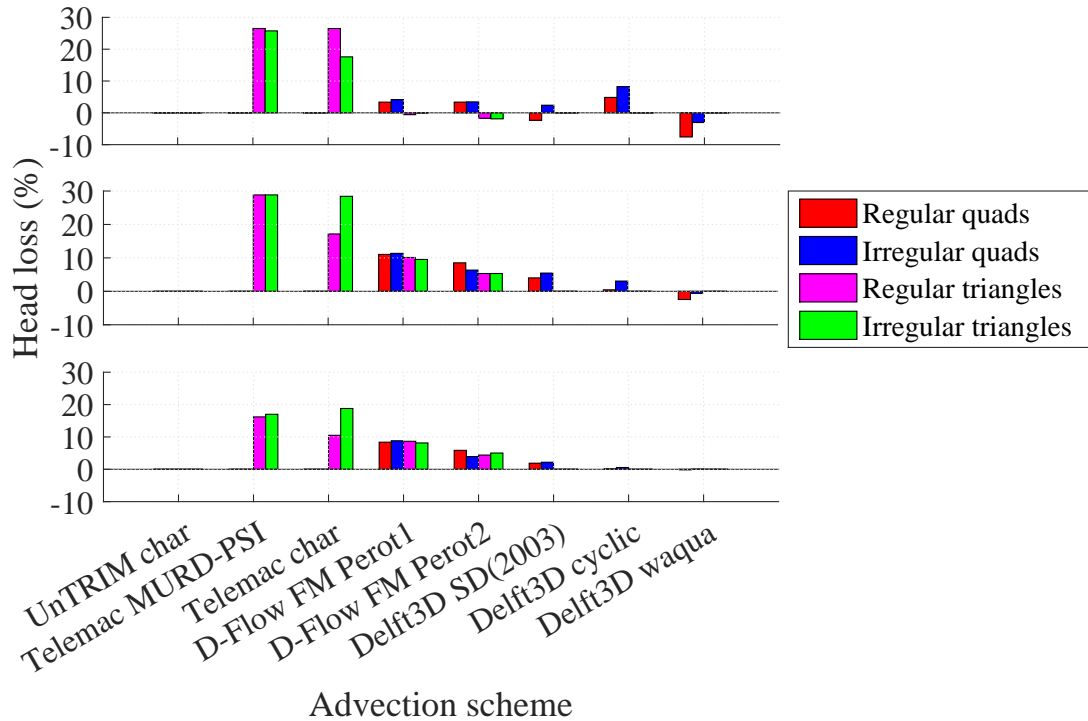


**Figure 6.5:** Numerical backwater for the flow over a sloped wavy bed test, for all advection schemes and grid structures, for the  $\Delta x \approx 10$  m (top),  $\Delta x \approx 5$  m (middle) and  $\Delta x \approx 2.5$  m (bottom) resolution grid.

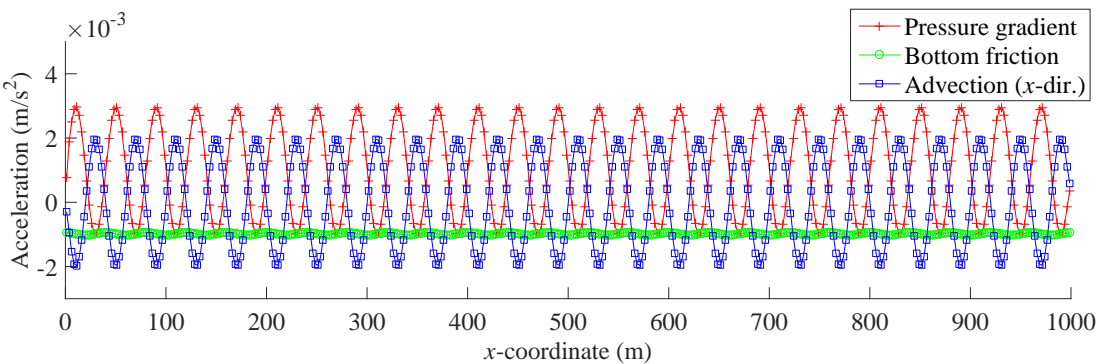


**Figure 6.6:** Different acceleration terms in the momentum equation along the channel centreline for the sloped wavy bed test with a reduced bed form amplitude  $A_b = 0.05$  m.

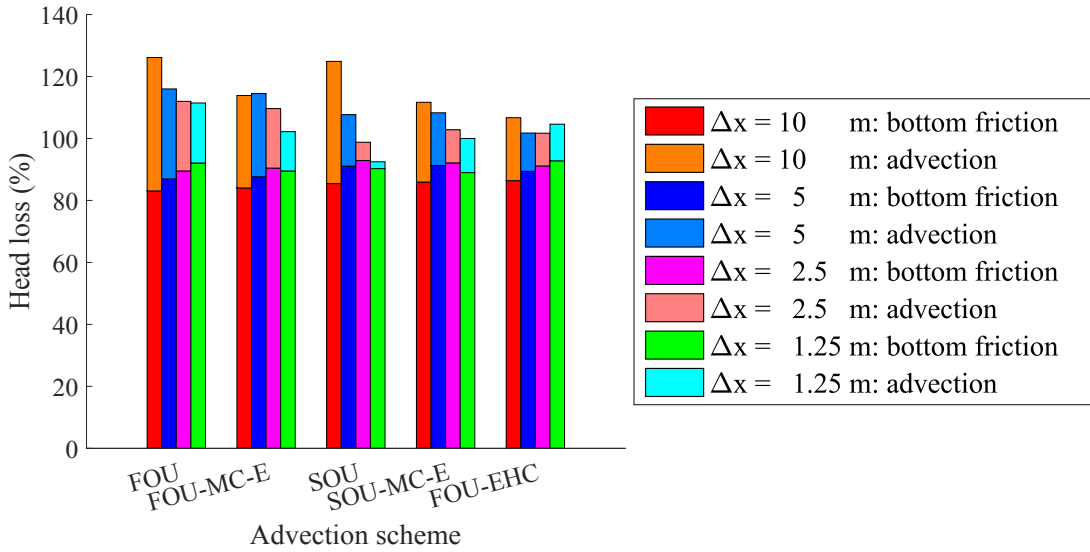


**Figure 6.7:** Percentual head loss for the flow over a sloped wavy bed with emerged groynes. Computations performed on a structured grid, using the five advection schemes from the analysis, and all four grid resolutions. Displayed is the total head loss as a sum of the head loss due to bottom friction and the head loss due to advection.

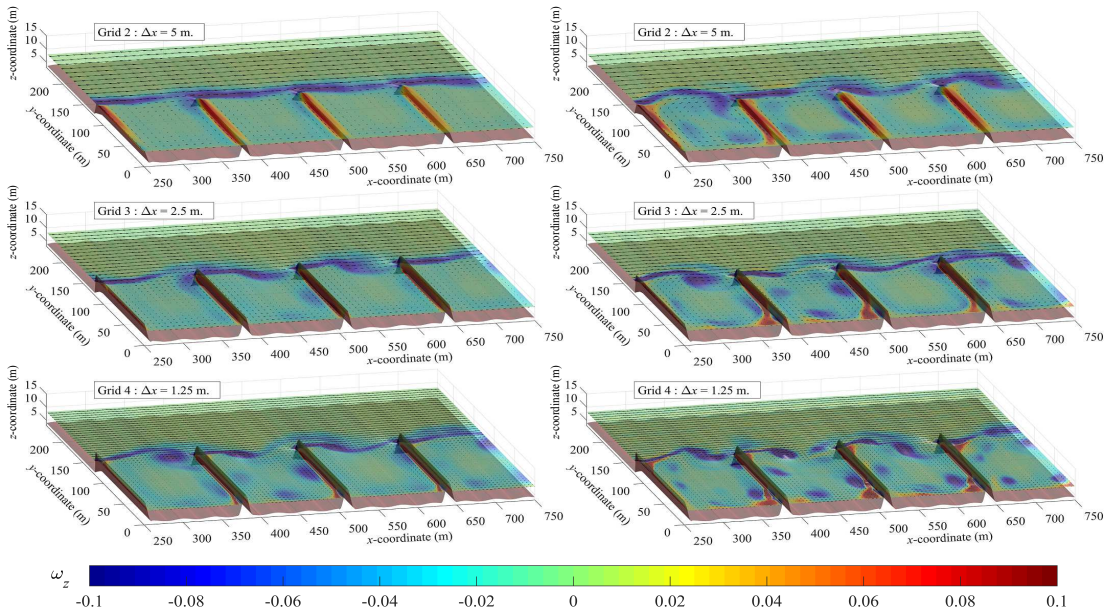


**Figure 6.8:** Flow around emerged groynes:  $z$ -component of the vorticity  $\vec{\omega}$  [ $s^{-1}$ ] around groynes 5, 6 and 7, superimposed on the free surface level, for the FOU-MC-E (left) and SOU-MC-E (right) advection scheme, for the three finest grids.

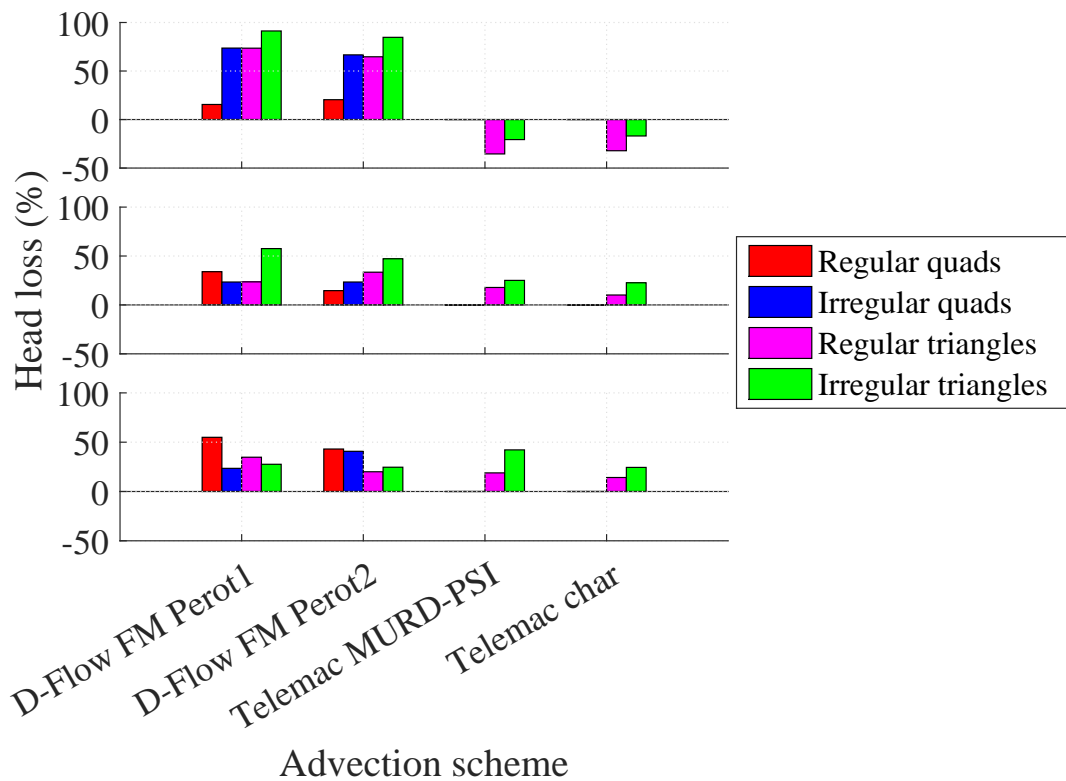


**Figure 6.9:** Numerical backwater for the flow over a sloped wavy bed with emerged groynes, for the advection schemes from D-Flow FM and Telemac and for the available grid structures, for the  $\Delta x \approx 10\text{ m}$  (top),  $\Delta x \approx 5\text{ m}$  (middle) and  $\Delta x \approx 2.5\text{ m}$  (bottom) resolution grid.

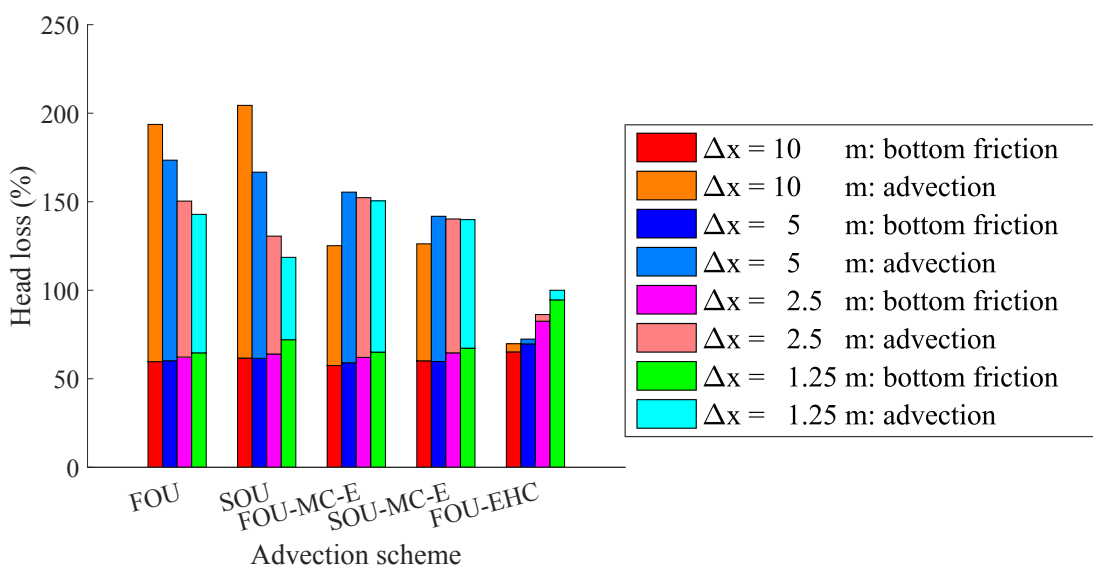


**Figure 6.10:** Artificial head loss for the flow over a sloped wavy bed with submerged groynes, for the five schematic advection schemes from the analysis and all four grid resolutions.

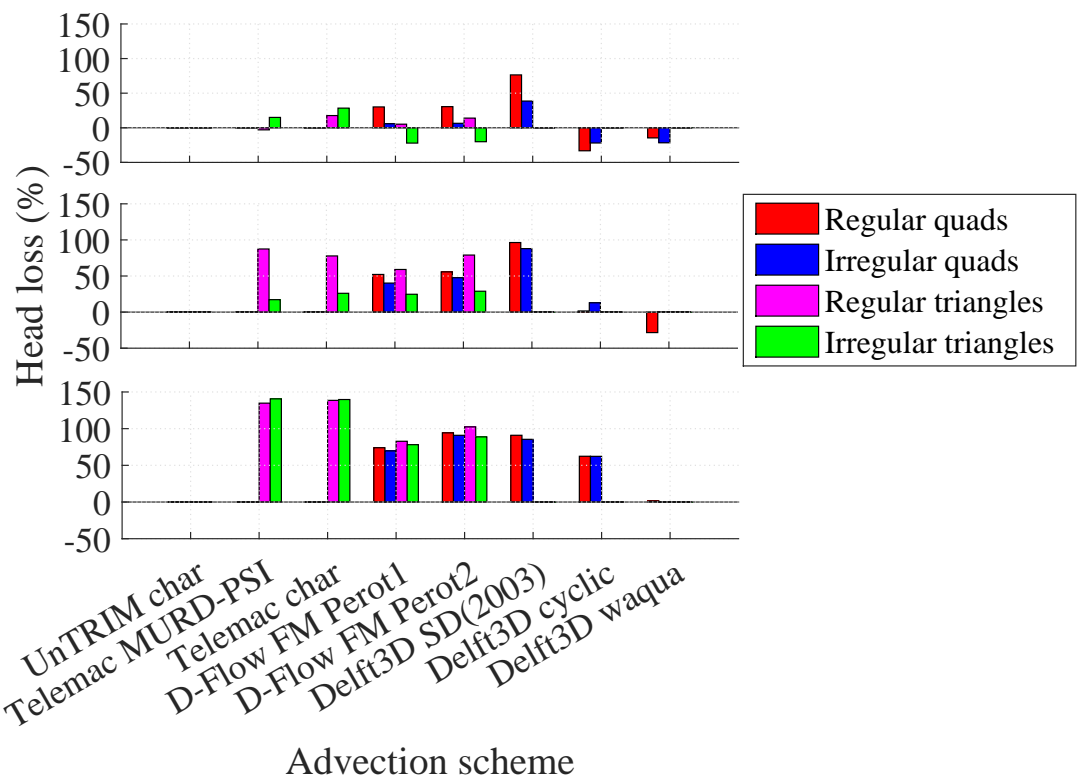


**Figure 6.11:** Artificial backwater due to advection for the flow over a sloped wavy bed test with submerged groynes, for all advection schemes and grid structures, for the 10 m (top), 5 m (middle) and 2.5 m (bottom) resolution grid.

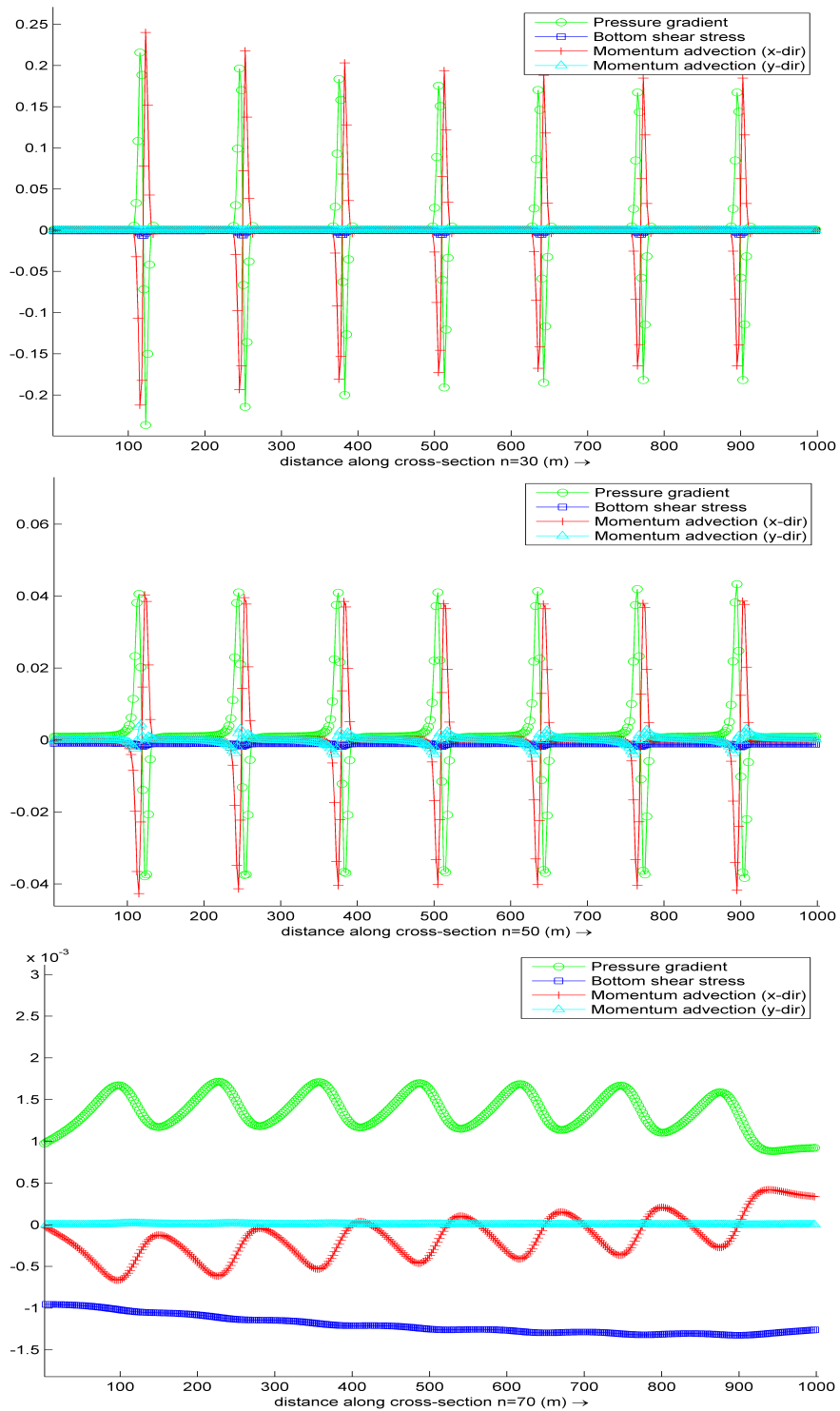


**Figure 6.12:** Different acceleration terms in the momentum equation for the sloped channel with groynes, for the longitudinal cross-sections at  $y = 75$  m over the groynes (top),  $y = 125$  m through the center of the channel, near the groyne tips (middle) and at  $y = 175$  m, in main channel (bottom). Note the different vertical scales.

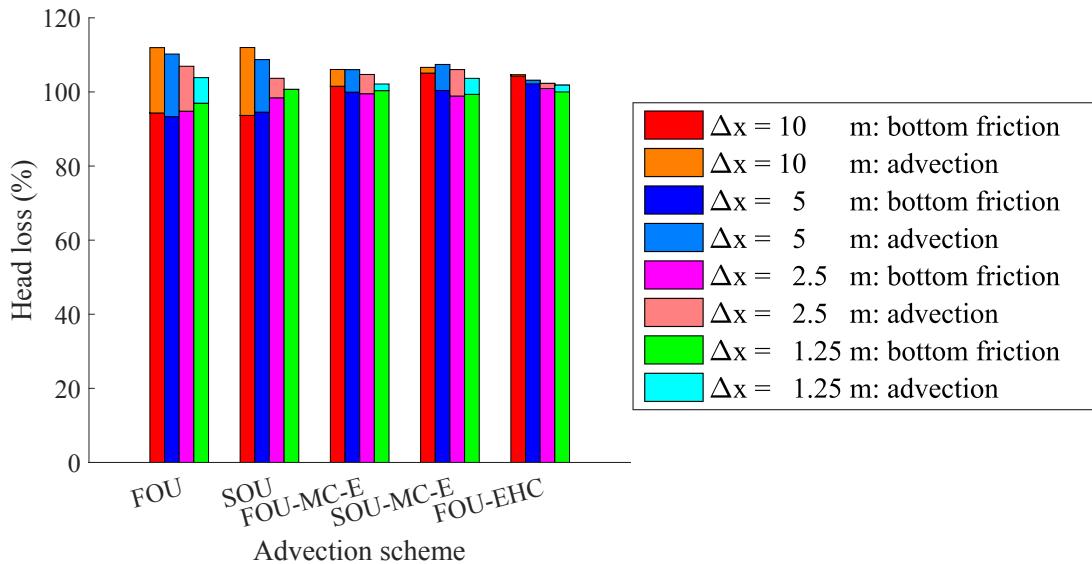


**Figure 6.13:** Percentual artificial head loss due to advection for the Elbe River test case, for the five schematic advection schemes from the analysis and all four grid resolutions.

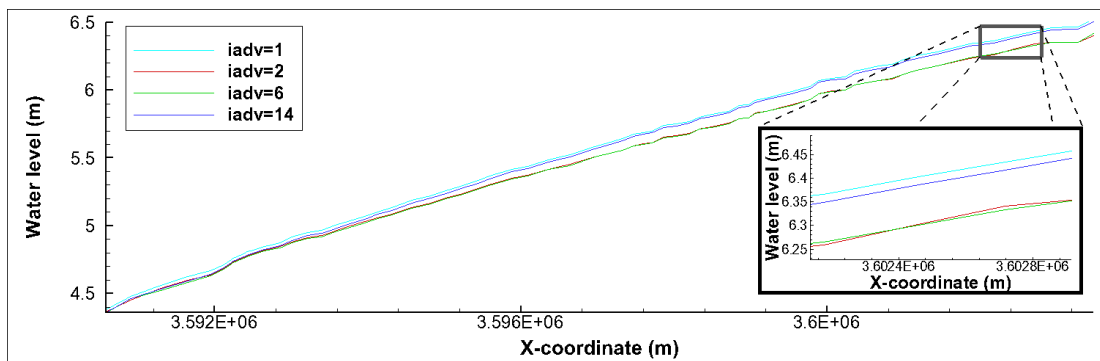


**Figure 6.14:** Elbe River from Lauenburg to Geesthacht. Water levels along the centerline of the river, obtained with Telemac on regular triangles for the four different advection schemes: 1) the characteristics scheme; 2) the SUPG scheme; 6) the MURD-N scheme (edge-by-edge); and 14) the MURD-PSI scheme.

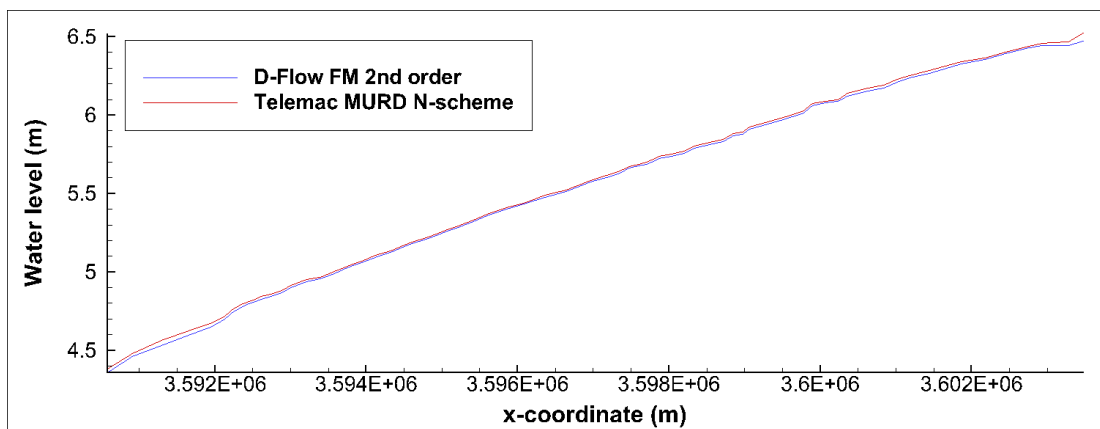


**Figure 6.15:** Elbe River from Lauenburg to Geesthacht. Water levels along the centerline of the river, obtained with Telemac on regular triangles with the MURD N-scheme and with D-Flow FM using the second-order accurate Perot scheme.

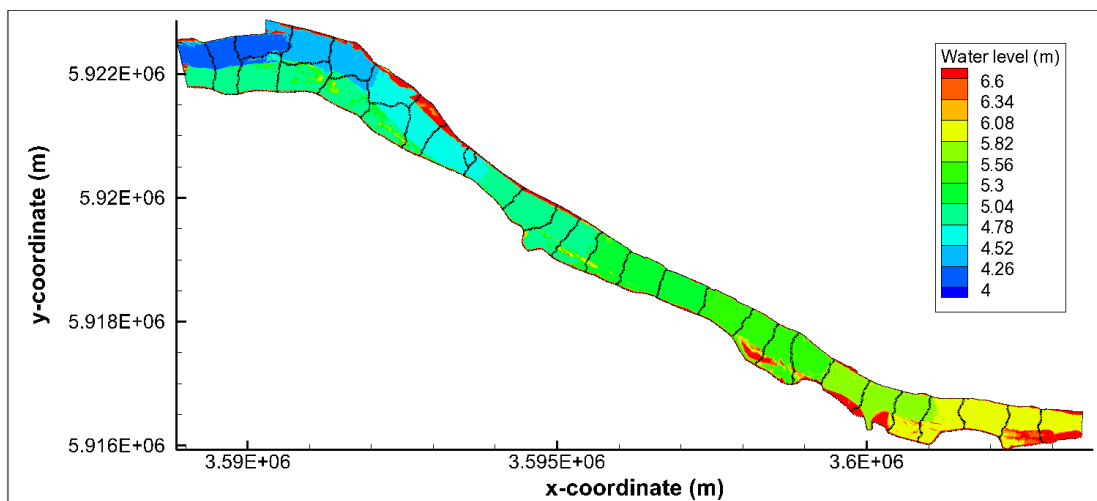


**Figure 6.16:** Elbe River from Lauenburg to Geesthacht. Water levels obtained with D-Flow FM on irregular triangles for the second-order accurate Perot scheme. The parallel (METIS) partitioning is also shown.

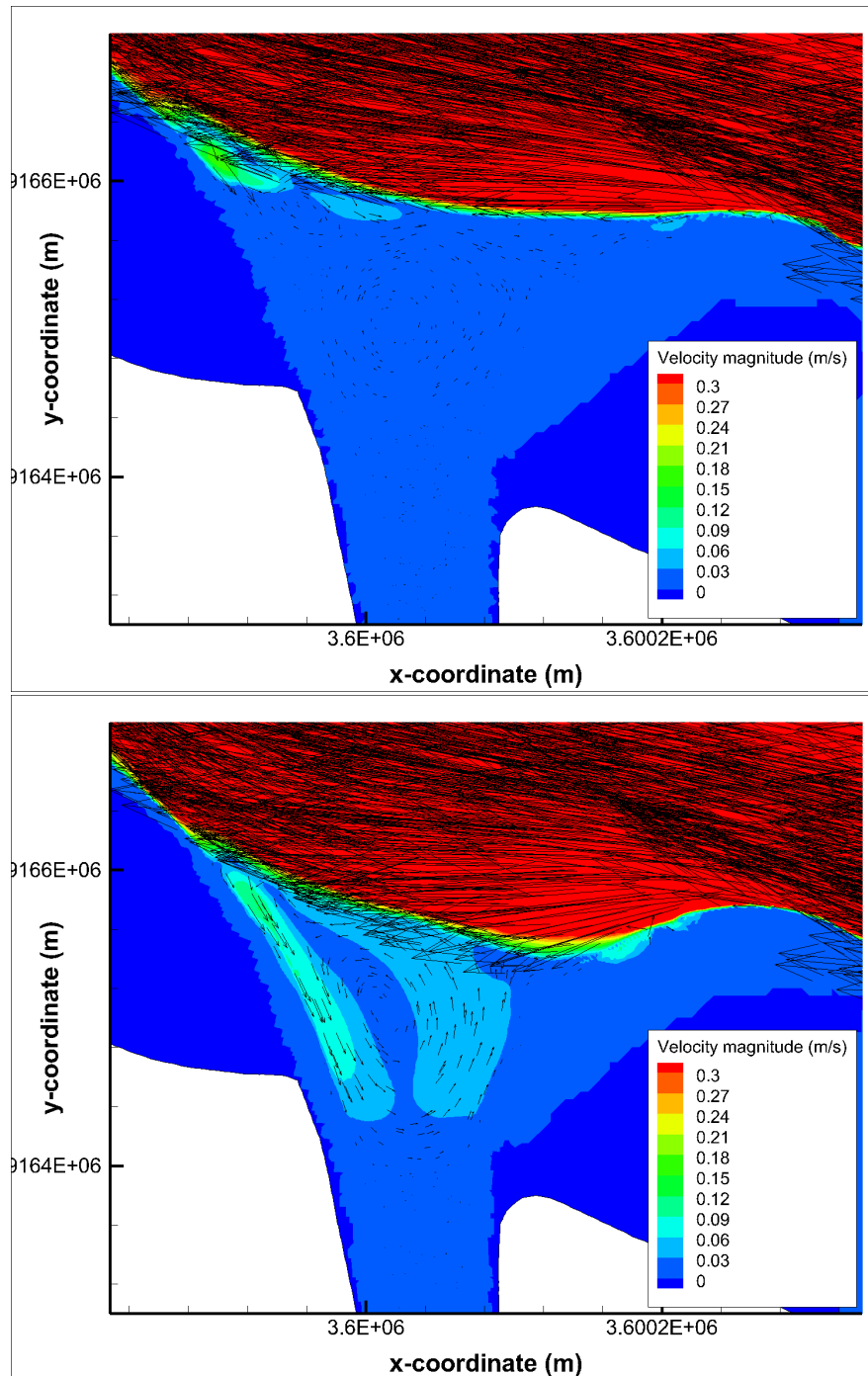


**Figure 6.17:** Elbe River from Lauenburg to Geesthacht. Velocities at the junction of the Elbe Side Channel and the Elbe river, obtained with Telemac on regular triangles for advection scheme 1 ("characteristics") at the top and 14 ("MURD N-scheme") at the bottom.



## 7 Discussion

It was shown that, for quasi-steady river flow over variable topography, the *local balance* in the momentum equation is dominated by the pressure gradient and advection term and not by the pressure gradient and bottom friction. Due to the errors in the advection scheme, even the contribution to the *global balance* may be substantial, depending on the chosen advection scheme and grid resolution. Therefore, the common consensus that rivers are dominated by a balance between pressure (or free-surface) gradient and bottom friction is often invalid when considering a numerical model. Already for relatively small bottom variations, the global contribution to the backwater due to inaccuracies of the advection scheme may be of the same order of magnitude as that from bottom friction.

This work considered the range of practically-feasible grid resolutions, where the geometrical variation is capturing with a limited number of cells, as large-scale river applications often require considerable computational resources. In comparison with classical test cases such as the “*subcritical flow over a bottom bump*”, we investigated a series of such bumps (and groynes), to allow for an accumulation of the possible numerical backwater that is introduced by the errors in the advection discretization.

In this work, the backwater effect for the flow over bed forms and influenced by groynes was considered. However, as any variation of the bathymetry may lead to artificial advection effects, it is very likely that this is also the case for the flow through bends, where similar investigations could be realized (e.g. [Blanckaert and Graf \(2004\)](#); [Blanckaert \(2010\)](#); [Van Balen et al. \(2010\)](#); [Stelling \(2012\)](#)). Also, in this study we restrict ourselves to quasi-steady flow with stationary boundary conditions. As can be seen from the presented results, the findings from this work also apply for mildly instationary flow situations.

In the present work a number of basic advection schemes were tested. It may be of interest to also apply other advection approximations to the presented set of test cases, inspired by a real-world river application, with the focus on the head loss and backwater. the investigations from this work can be realized on locally-refined grids, where the discretization errors from the advection scheme will interact with the transitions in the grid structure and resolution.

The Eulerian-Lagrangian scheme (both schematic and in Telemac and UnTRIM) also performs well, even for Courant numbers moderately above 1. It does give a relatively large contribution to the backwater. Several tests (not shown) with  $C = 2$ , demonstrate that both for the emerged and submerged groyne test and for the Elbe River case, similar results can be obtained.

The effect of the grid structure was identified to be moderate. For all the present applications, the introduction of grid irregularity did not strongly deteriorate the results. It might be that this conclusion is different for other tests or applications, where other balances (e.g. involving turbulent diffusion) are more important.



## 8 Conclusions

The aim of the work was to assess the quality of presently applied numerical models (and methods) concerning the accurate representation of water levels (backwater) in rivers with variable topography, such as bed forms and groynes. To quantify the accuracy of such numerical models, we provide a new interpretation of discretization errors in numerical river models, introducing the concept of numerical or artificial backwater. The artificial backwater effect due to the momentum advection approximation was quantified both on structured and unstructured/irregular grids. On structured rectangular grids we investigated three first-order advection schemes using a 1D analysis and verified the analysis using a sequence of 2D numerical experiments for the same schemes and for two second-order accurate extensions. On unstructured grids, four different numerical modelling systems were considered, allowing different grid structures (quadrilateral and triangular). Hybrid grids have not yet been considered. The considered modelling systems are Telemac, D-Flow FM, Delft3D and UnTRIM. For each system, several of the available advection schemes were tested for their influence on the (numerical) backwater.

### 8.1 Rectangular discretizations

We demonstrated that a scheme designed for maintaining constant energy head, can indeed compute the flow over variable topography with minimal energy losses. It was also shown that – in agreement with the conclusions from [Stelling and Duinmeijer \(2003\); Kramer and Stelling \(2008\)](#) – the artificial backwater for the momentum-conservative scheme cannot be controlled. The scheme gives an energy loss (positive backwater contribution) at expansions and an energy gain (negative backwater contribution) for contractions. For most flow/topography situations, however, the momentum-conservative scheme results in a smaller artificial backwater than the non-conservative first-order upwind FOU scheme.

These findings are confirmed by the numerical experiments, where the contributions to the global backwater from bottom friction and from the advection scheme have been computed. The scheme with energy-head constancy indeed shows very little to no backwater, but unfortunately shows this property also for flows where losses might be expected, such as for the flow over groynes. The non-conservative first-order upwind scheme was found to cause an artificial backwater effect that could be as high as 35% of the backwater due to bottom friction. In agreement with the 1D analysis, the momentum-conservative scheme shows less backwater than the FOU scheme.

Tests with the second-order extensions of the schemes – showed that the non-conservative second-order scheme does show faster convergence than the FOU scheme, but on coarser grids, the backwater is even larger than with the FOU scheme. It was shown that first-order advection schemes that adhere to physical principles, such as momentum conservation or energy-head constancy along streamlines, give less artificial backwater than a higher-order scheme that does not adhere to such principles.

## 8.2 Irregular/unstructured discretizations

As could be expected, the first- and second-order accurate Perot schemes in D-Flow FM show similar characteristics as the tested schematic momentum-conservative schemes.

The advection schemes from the Telemac system showed more artificial backwater for the schematic numerical tests. The difference with the less dissipative advection schemes was found to be up to a factor of two, resulting in several decimeters of water level difference. This large difference was not found for the Elbe river case study.

The effect of the grid structure was identified to be moderate. For all the present applications, the introduction of grid irregularity did not strongly deteriorate the results. It might be that this conclusion is different for other tests or applications, where other balances (e.g. involving turbulent diffusion) are more important.

## 8.3 General conclusions

At present, most river computations employ moderately coarse grids, where the topography is resolved with limited resolution and the size of the artificial backwater considerably depends on the chosen advection scheme. From the schemes and systems investigated in the present work – for computations at the applied resolutions – the authors recommend the use of a momentum-conservative first-order scheme or a scheme with energy-head constancy, for their efficiency and insensitivity to the grid resolution. Only for higher resolutions – where accurate flow patterns need to be resolved (e.g. including vortex shedding) – a second-order momentum-conservative scheme is recommended.

## 9 Outlook

In this work, we considered several basic advection schemes and a number of more sophisticated advection schemes (but still at most third order accurate) available in the modelling systems Telemac, D-Flow Flexible Mesh, Delft3D and UnTRIM. In these systems there are still several advection schemes that have not yet been tested. It might be interesting to see how these schemes perform for the tests presented in this work. Additionally, the focus on the head loss and backwater may be of interest for other type of models that handle the advection terms in a different way, e.g. based on Godunov schemes, Riemann solvers, using (W)ENO approximations or Discontinuous Galerkin approaches.

In particular in the context of the modellings systems that do not require orthogonal grids (e.g. Telemac), it may of interest to investigate the effect of the grid orthogonality on the results.

Considering the convergence properties of the considered schemes, it might be interesting to investigate the effect of local instead of global grid refinement, e.g. around groynes, as is common practise in river engineering projects. Additionally, the effect of transitions in grid structure, e.g. from quadrilaterals to triangles or vice versa, could be considered for their effect on the backwater (i.e. hybrid grids).

In this work, the applied grids were fine enough to (just) resolve the topographic features we were investigating (bed forms and groynes). Often, due to computational resources, the computational grids are still so coarse, that *subgrid* schematizations need to be applied, to incorporate the resistance and *flow steering* effects of such topographic features. For instance, the addition of certain energy (e.g. Carnot) losses at grid cells/edges where weirs/groynes are positioned (but not resolved), is common practice for many river engineers. This modelling strategy can be compared for its accuracy and consistency (e.g. for modelling the effect of lowering groynes), with the present investigations.

In this work, the effect of the application of the subgrid method presented by Casulli (2009); Casulli and Stelling (2011) and further developed by Stelling (2012); Volp *et al.* (2013); Sehili *et al.* (2014); Platzek *et al.* (2016), where high-resolution topography can be efficiently included in a (coarse-grid) hydrodynamic model, was not presented. Several preliminary tests were, however, performed. The effect of the subgrid method on the results is not clear yet and requires further investigation.



## 10 Final remarks

Many modellers believe that the momentum advection scheme is of secondary importance in river computations. However, it is shown that the choice of the advection scheme can considerably influence the model results. In particular, the discretization errors from the advection scheme can contribute to the global backwater, deteriorating the confidence in model results.

Most modellers, project managers and (to a lesser extent) developers, however, are not aware of this effect and have great faith in model outcomes, without a critical look at the input or the model implementation. This conception can lead to situations where important engineering conclusions are drawn from erroneous model results. To avoid such situations, a fair amount of scepticism is required. The idea was to create awareness by the reader (modeller, manager, developer or a different kind), that the momentum advection scheme is not to be taken for granted.



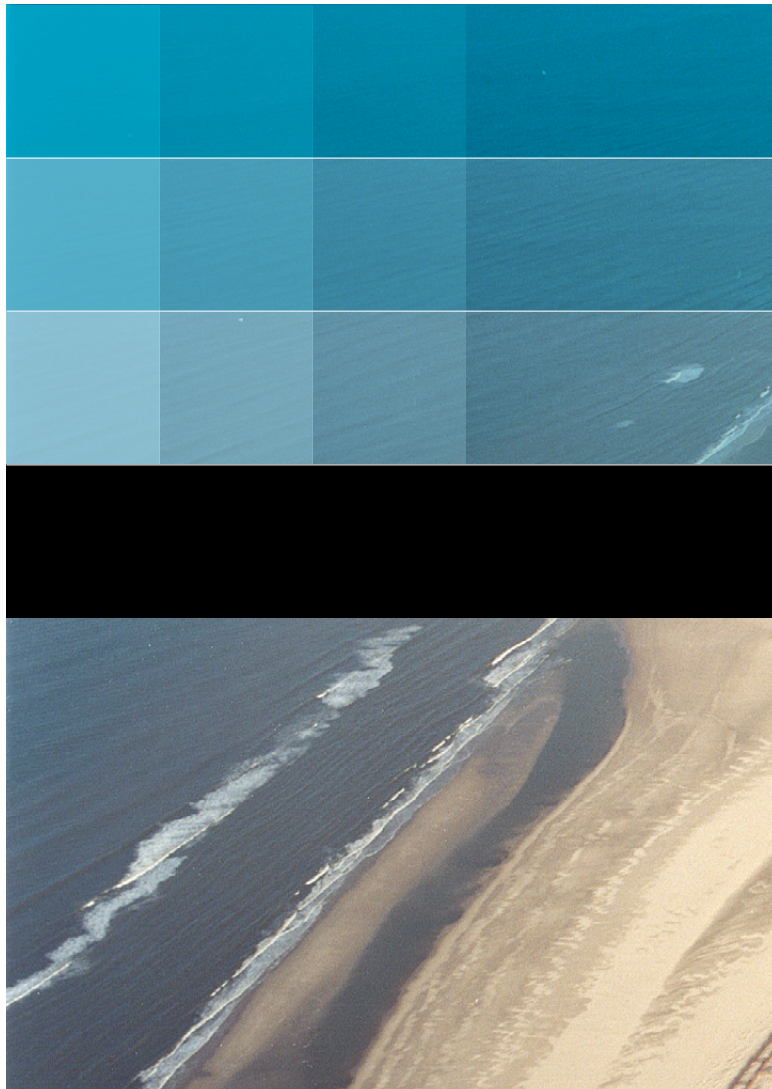
- Abgrall, R. and M. Mezine, 2003. "Construction of second order accurate monotone and stable residual distribution schemes for unsteady flow problems." *Journal of Computational Physics* 188: 16–55. DOI: 10.1016/S0021-9991(03)00084-6.
- Blanckaert, K., 2010. "Topographic steering, flow recirculation, velocity redistribution, and bed topography in sharp meander bends." *Water Resources Research* 46 (9): 1–23. ISSN 1944-7973.
- Blanckaert, K. and W. H. Graf, 2004. "Momentum Transport in Sharp Open-Channel Bends." *Journal of Hydraulic Engineering* 130 (3): 186–198.
- Blumberg, A. F. and G. L. Mellor, 1987. *A Description of a Three-Dimensional Coastal Ocean Circulation Model*, pages 1–16. American Geophysical Union.
- Brunner, G., 2016. "HEC-RAS River Analysis System, Hydraulic Reference Manual 5.0." US Army Corps of Engineers, Davis, CA, USA. 538 pp.
- Busnelli, M. M., F. Schuurman, A. Sieben, M. van der Wal and H. Hector, 2011. "Morphodynamic responds of groyne fields to the lowering of crest level of the groynes in the Waal River, The Netherlands." In *River, Coastal and Estuarine Morphodynamics: RCEM2011*, The 7th IAHR Symposium on River, Coastal and Estuarine Morphodynamics, Sept. 6–8, page 1450–1463. Tsinghua University Press, Beijing.
- Caleffi, V. and A. Valiani, 2009. "Well-Balanced Bottom Discontinuities Treatment for High-Order Shallow Water Equations WENO Scheme." *Journal of Engineering Mechanics* 135 (7): 684–696.
- Caleffi, V., A. Valiani and G. Li, 2016. "A comparison between bottom-discontinuity numerical treatments in the DG framework." *Applied Mathematical Modelling* 40: 7516–7531.
- Canestrelli, A. and E. Toro, 2012. "Restoration of the contact surface in FORCE-type centred schemes II: Non-conservative one- and two-layer two-dimensional shallow water equations." *Advances in Water Resources* 47: 76–87.
- Casulli, V., 1990. "Semi-implicit finite difference methods for the two-dimensional shallow water equations." *J. Comput. Phys.* 86 (1): 56–74. ISSN 0021-9991.
- Casulli, V., 2009. "A high-resolution wetting and drying algorithm for free-surface hydrodynamics." *International Journal for Numerical Methods in Fluids* 60 (4): 391–408.
- Casulli, V. and E. Cattani, 1994. "Stability, Accuracy and Efficiency of a semi-implicit method for three-dimensional shallow water flow." *Computers Math. Applic* 27 (4): 99–112.
- Casulli, V. and R. T. Cheng, 1990. "Stability analysis of Eulerian-Lagrangian methods for the one-dimensional shallow-water equations." *Applied Mathematical Modelling* 14: 122–131.
- Casulli, V. and R. T. Cheng, 1992. "Semi-implicit finite difference methods for three-dimensional shallow water flow." *Int. J. Numer. Meth. Fluids* 15 (6): 629–648.
- Casulli, V. and G. S. Stelling, 2011. "Semi-implicit subgrid modelling of three-dimensional free-surface flows." *International Journal for Numerical Methods in Fluids* 67 (4): 441–449.
- Casulli, V. and R. Walters, 2000. "An unstructured grid, three-dimensional model based on the shallow water equations." *International Journal for Numerical Methods in Fluids* 32 (3): 331–348. DOI: 10.1002/(SICI)1097-0363(20000215)32:3<331::AID-FLD941>3.0.CO;2-C.
- Casulli, V. and P. Zanolli, 2002. "Semi-implicit numerical modeling of nonhydrostatic free-surface flows for environmental problems." *Math. Comput. Model* 36 (9-10): 1131–1149.

- Chanson, H., 2004. *The hydraulics of open channel flow*. Butterworth-Heinemann, Oxford, 2nd ed.
- Chanson, H., 2009. "Development of the Bélanger Equation and Backwater Equation by Jean-Baptiste Bélanger (1828)." *Journal of Hydraulic Engineering* 135 (3): 159–163.
- Deltares, 2013. "Delft3D-FLOW: Simulation of multi-dimensional hydrodynamic flows and transport phenomena, including sediments. User Manual version 3.14." 672 pp.
- DHI, 2011. "MIKE 21 C Curvilinear Model, Scientific Documentation. Mike by DHI." 112 pp.
- Fringer, O. B., M. Gerritsen and R. L. Street, 2006. "An unstructured-grid, finite-volume, nonhydrostatic, parallel coastal ocean simulator." *Ocean Modelling* 14: 139–173. DOI: [10.1016/j.ocemod.2006.03.006](https://doi.org/10.1016/j.ocemod.2006.03.006).
- Galland, J.-C., N. Goutal and J.-M. Hervouet, 1991. "TELEMAC: A new numerical model for solving shallow water equations." *Advances in Water Resources* 14 (3): 138-148.
- Ham, D. A., J. D. Pietrzak and G. S. Stelling, 2006. "A streamline tracking algorithm for semi-Lagrangian advection schemes based on the analytic integration of the velocity field." *J. Comput. Appl. Math.* 192 (1): 168-174. DOI: [10.1016/j.cam.2005.04.055](https://doi.org/10.1016/j.cam.2005.04.055), ISSN 0377-0427.
- Hervouet, J.-M., 2007. *Hydrodynamics of free surface flows - modelling with the finite element method*. John Wiley & Sons Ltd.
- Hervouet, J.-M. and J. Jankowski, 2000. "Comparing numerical simulations of free surface flows using non-hydrostatic Navier-Stokes and Boussinesq equations." In *Proceedings of the 4th Conference on Hydroinformatics*. Iowa City, Iowa (USA).
- Jankowski, J., 1999. *A Non-Hydrostatic Model for Free Surface Flows*. Bericht nr. 56, Institut fuer Stroemungsmechanik.
- Kernkamp, H. W. J., A. van Dam, G. S. Stelling and E. D. de Goede, 2011. "Efficient scheme for the shallow water equations on unstructured grids with application to the Continental Shelf." *Ocean Dynamics* 61 (8): 1175–1188. ISSN 1616-7228.
- Kleptsova, O., J. D. Pietrzak and G. S. Stelling, 2012. "On a momentum conservative  $z$ -layer unstructured C-grid ocean model with flooding." *Ocean Dynamics* 54-55: 18–36.
- Kleptsova, O., G. S. Stelling and J. D. Pietrzak, 2010. "An accurate momentum advection scheme for a  $Z$ -level coordinate models." *Ocean Dynamics* 60 (6): 1447–1461. ISSN 1616-7341.
- Kramer, S. C. and G. S. Stelling, 2008. "A conservative unstructured scheme for rapidly varied flows." *International Journal for Numerical Methods in Fluids* 58 (2): 183–212.
- Leendertse, J., 1967. *Aspects of a computational model for long-period water-wave propagation*. Memorandum RM-5294-PR, Rand Corporation, Santa Monica, USA.
- Noelle, S., Y. Xing and C.-W. Shu, 2007. "High-order well-balanced finite volume WENO schemes for shallow water equation with moving water." *Journal of Computational Physics* 226 (1): 29–58. DOI: <http://dx.doi.org/10.1016/j.jcp.2007.03.031>, ISSN 0021-9991.
- Perot, B., 2000. "Conservation properties of unstructured staggered mesh schemes." *J. Comp. Phys.* 159: 58–89.
- Platzek, F. W., G. S. Stelling, J. A. Jankowski, R. Patzwahl and J. D. Pietrzak, 2016. "An efficient semi-implicit subgrid method for free-surface flow on hierarchical grids." *Int. J. Numer. Meth. Fluids* 80 (12): 715–741.

- Ricchiuto, M., 2015. "An explicit residual based approach for shallow water flows." *Journal of Computational Physics* 280: 306–344. ISSN 0021-9991.
- Ricchiuto, M., R. Abgrall and H. Deconinck, 2007. "Application of Conservative Residual Distribution Schemes to the Solution of the Shallow Water Equations on Unstructured Meshes." *J. Comput. Phys.* 222 (1): 287–331. DOI: [10.1016/j.jcp.2006.06.024](https://doi.org/10.1016/j.jcp.2006.06.024), ISSN 0021-9991.
- Ricchiuto, M. and A. Bollermann, 2009. "Stabilized residual distribution for shallow water simulations." *Journal of Computational Physics* 228 (4): 1071–1115. DOI: [10.1016/j.jcp.2008.10.020](https://doi.org/10.1016/j.jcp.2008.10.020), ISSN 0021-9991.
- Sehili, A., G. Lang and C. Lippert, 2014. "High-resolution subgrid models: background, grid generation, and implementation." *Ocean Dynamics* 64 (4): 519–535. DOI: [10.1007/s10236-014-0693-x](https://doi.org/10.1007/s10236-014-0693-x), ISSN 1616-7341.
- Staniforth, A. and J. Côté, 1991. "Semi-Lagrangian integration schemes for atmospheric models - A review." *Monthly Weather Review* 119: 2206–2223.
- Stelling, G. S., 1983. *On the construction of computational methods for shallow water flow problems*. Ph.D. thesis, Technische Hogeschool Delft, Delft, Netherlands. DOI: <http://repository.tudelft.nl/view/ir/uuid%3Ad3b818cb-9f91-4369-a03e-d90c8c175a96/>.
- Stelling, G. S., 2012. "Quadtree flood simulations with sub-grid digital elevation models." *Proceedings of the ICE - Water Management* 165 (WM10): 567–580.
- Stelling, G. S. and S. P. A. Duinmeijer, 2003. "A staggered conservative scheme for every Froude number in rapidly varied shallow water flows." *International Journal for Numerical Methods in Fluids* 43: 1329–1354.
- Stelling, G. S. and J. J. Leendertse, 1992. "Approximation of convective processes by cyclic AOI methods." In M. Spaulding, K. Bedford and A. Blumberg, eds., *Estuarine and coastal modeling; proceedings of the 2nd international conference*, pages 771–782. American Society of Civil Engineers.
- Toro, E. F. and P. Garcia-Navarro, 2007. "Godunov-type methods for free-surface shallow flows: A review." *Journal of Hydraulic Research* 45 (6): 736–751.
- Van Balen, W., W. S. J. Uijttewaal and K. Blanckaert, 2010. "Large-eddy simulation of a curved open-channel flow over topography." *Physics of Fluids* 22 (7): 18. DOI: [10.1063/1.3459152](https://doi.org/10.1063/1.3459152).
- Volp, N. D., B. C. V. Prooijen and G. S. Stelling, 2013. "A finite volume approach for shallow water flow accounting for high-resolution bathymetry and roughness data." *Water Resour. Res.* 49 (7): 4126–4135.
- Weilbeer, H., J. A. Jankowski and W. Zielke, 1999. "A three-dimensional non-hydrostatic model for free surface flows - development, verification and limitations." In M. Spaulding and R. Cheng, eds., *Estuarine and Coastal Modelling*, Proceedings of the 6th International Conference. ASCE.
- Zhang, D., C. Jiang, D. Liang and L. Cheng, 2015. "A review on TVD schemes and a refined flux-limiter for steady-state calculations." *Journal of Computational Physics* 302: 114–154.
- Zijlema, M., 1999. *Technical documentation TRIWAQ*. Technical Report SIMONA 99-01, National Institute for Coastal and Marine Management, The Hague, The Netherlands.







# Deltares systems

PO Box 177  
2600 MH Delft  
Rotterdamseweg 185  
2629 HD Delft  
The Netherlands

+31 (0)88 335 81 88  
[sales@deltaressystems.nl](mailto:sales@deltaressystems.nl)  
[www.deltaressystems.nl](http://www.deltaressystems.nl)